

The Milky Way’s stellar streams and globular clusters do not align in a Vast Polar Structure

Alexander H. Riley^{1,2}★ and Louis E. Strigari^{1,2}

¹*George P. and Cynthia Woods Mitchell Institute for Fundamental Physics and Astronomy, Texas A&M University, College Station, TX 77843, USA*

²*Department of Physics and Astronomy, Texas A&M University, College Station, TX 77843, USA*

Accepted 2020 March 9. Received 2020 March 6; in original form 2020 January 30

ABSTRACT

There is increasing evidence that a substantial fraction of Milky Way satellite galaxies align in a rotationally-supported plane of satellites, a rare configuration in cosmological simulations of galaxy formation. It has been suggested that other Milky Way substructures (namely young halo globular clusters and stellar/gaseous streams) similarly tend to align with this plane, accordingly dubbed the Vast Polar Structure (VPOS). Using systemic proper motions inferred from *Gaia* data, we find that globular cluster orbital poles are not clustered in the VPOS direction, though the population with the highest VPOS membership fraction is the young halo clusters (~30%). We additionally provide a current census of stellar streams, including new streams discovered using the Dark Energy Survey and *Gaia* datasets, and find that stellar stream normals are also not clustered in the direction of the VPOS normal. We also find that, based on orbit modeling, there is a likely association between NGC 3201 and the Gjöll stellar stream and that, based on its orbital pole, NGC 4147 is likely not a Sagittarius globular cluster. That the Milky Way’s accreted globular clusters and streams do not align in the same planar configuration as its satellites suggests that the plane of satellites is either a particularly stable orbital configuration or a population of recently accreted satellites. Neither of these explanations is particularly likely in light of other recent studies, leaving the plane of satellites problem as one of the more consequential open problems in galaxy formation and cosmology.

Key words: galaxies: kinematics and dynamics – Local Group – galaxies: formation

1 INTRODUCTION

For over 40 years, it has been known that the classical¹ satellites of the Milky Way fall on the same polar great circle as the Magellanic Stream (Lynden-Bell 1976; Kunkel & Demers 1976). More recent studies have confirmed the existence of the Milky Way’s plane of satellites (Lynden-Bell 1982; Kroupa et al. 2005; Metz et al. 2007) and found that the orbital poles of its constituents cluster in the same direction as the spatial plane (Metz et al. 2008; Pawlowski & Kroupa 2013), establishing the plane of satellites as a stable, co-rotating system. Similarly thin, kinematically-coherent satellite planes have been observed around M31 (Conn et al. 2013; Ibata et al. 2013; Santos-Santos et al. 2019) and Centaurus A (Müller et al. 2018), with contested statistical evidence of such systems around more distant host galaxies (Ibata et al. 2014a, 2015; Cautun et al. 2015a; Phillips et al. 2015).

Particular attention has been paid to the Milky Way’s plane of

satellites, as it is the system with the most information and highest quality data by nature of our place as observers. As more (and fainter) satellite galaxies have been discovered in the Sloan Digital Sky Survey, the Dark Energy Survey, and smaller community efforts (Simon 2019), these new satellites continue to preferentially reside in the same spatial plane (Metz et al. 2009a; Pawlowski & Kroupa 2014; Pawlowski et al. 2015a). Proper motion measurements using data from *Gaia* Data Release 2 (DR2; Gaia Collaboration et al. 2018a) show that the orbital poles for non-classical satellites also preferentially cluster in this plane (Fritz et al. 2018). Overall, 19 of the 41 satellites with 6-D phase-space measurements have orbital poles that align with the VPOS, while an additional 10 have insufficient proper motion accuracy to establish whether they align. Furthermore, the degree of kinematic coherence for the classical satellites has increased as measurements continue to improve, as expected if the underlying distribution was truly correlated (Pawlowski & Kroupa 2020).

Most notably, Pawlowski et al. (2012) found that Milky Way stellar/gaseous streams and the spatial distribution of young halo globular clusters preferentially align with the satellite galaxy plane. This dramatically strengthened the case for highly-correlated structure formation in the Milky Way, connecting three different sets of accreted objects. Since this finding, the Milky Way’s planar struc-

★ E-mail: alexriley@tamu.edu. Code for this work is available on [Github](#).

¹ Throughout this work, “classical” refers to the 11 Milky Way satellites discovered prior to the Sloan Digital Sky Survey: Carina, Draco, Fornax, Leo I and II, the Large and Small Magellanic Clouds, Sagittarius, Sculptor, Sextans, and Ursa Minor.

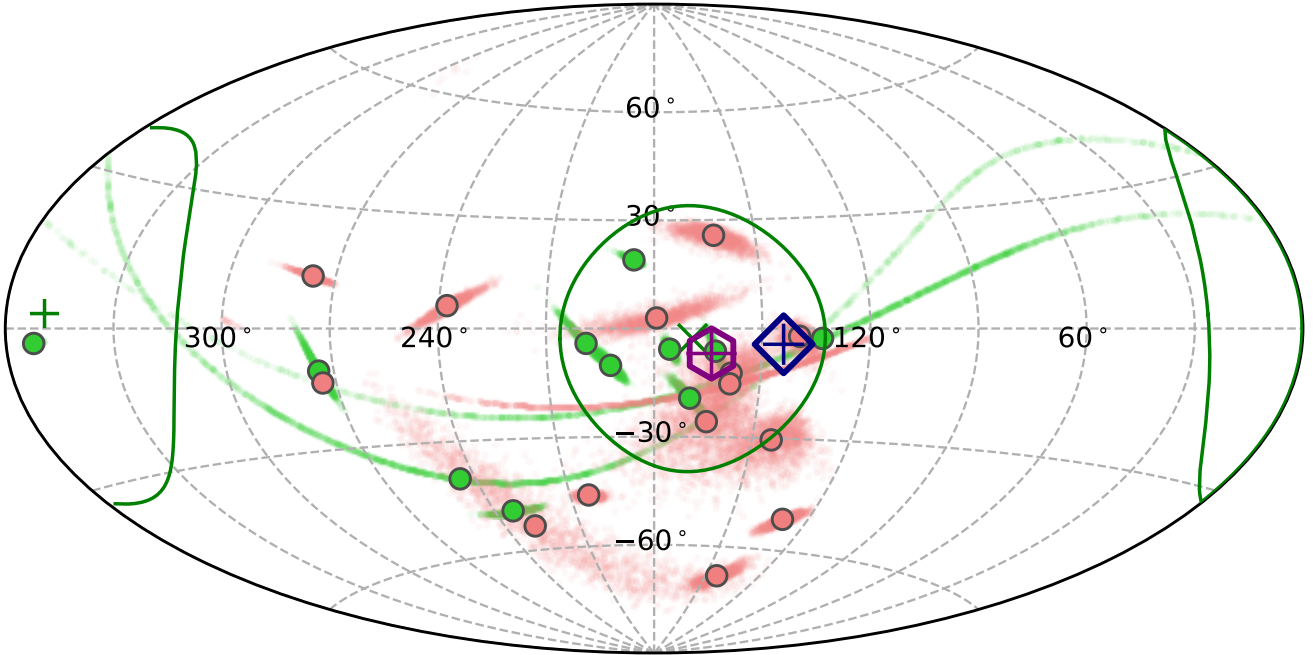


Figure 1. All-sky distribution of orbital poles for Milky Way classical satellites (green) and normals for stellar and gaseous streams discovered prior to 2012 (Pawlowski et al. 2012, red) in an Aitoff projection. We use spherical coordinates $(l_{\text{MW}}, b_{\text{MW}})$ that are aligned with the heliocentric Galactic system and centered on the Milky Way center (Pawlowski & Kroupa 2020). Orbital poles for the satellites are calculated as described in Section 2.1 using data compiled by Riley et al. (2019). Since the orbital sense is unknown for most streams, only one of the two stream normals (those from $120^\circ < l_{\text{MW}} < 300^\circ$) is shown. The large points correspond to the observed (assuming no measurement errors) orbital poles, while the point clouds show the results of 2,000 Monte Carlo simulations incorporating measurement errors. We also show the normal vector of a disk fitted to the spatial distribution of young halo globular clusters (Pawlowski et al. 2012, blue diamond) and the minor axis direction of a spatial plane fitted to all Milky Way satellites (Pawlowski et al. 2015a, purple hexagon). The green circles each contain 10% of the sky around the assumed VPOS pole (Pawlowski & Kroupa 2013; Fritz et al. 2018), given as an “x” for the co-orbiting direction and a “+” for the counter-orbiting direction. *The previously observed preferential alignment of Milky Way satellite galaxies, stellar streams, and young halo globular clusters has been dubbed the Vast Polar Structure (VPOS).*

ture has usually been referred to as the Vast Polar Structure (VPOS), comprised of satellite galaxies, globular clusters, and stellar streams.

Satellite planes as thin and kinematically correlated as observed in the Milky Way are extremely rare in cosmological simulations (Ibata et al. 2014b; Pawlowski et al. 2014; Cautun et al. 2015b; Shao et al. 2019), posing a small-scale challenge to our current Λ CDM cosmological paradigm (Bullock & Boylan-Kolchin 2017). All proposed solutions within Λ CDM have, thus far, not been able to explain such kinematic coherence satisfactorily, including: infall of satellites in groups (D’Onghia & Lake 2008; Metz et al. 2009b; Wang et al. 2013; Shao et al. 2018), accretion along a cosmic filament (Zentner et al. 2005; Lovell et al. 2011; Libeskind et al. 2011; Pawlowski et al. 2014), the inclusion baryonic effects in cosmological simulations (Pawlowski et al. 2015b; Ahmed et al. 2017; Müller et al. 2018; Pawlowski et al. 2019), and special environments or properties of the host halos (Pawlowski & McGaugh 2014; Buck et al. 2015; Pawlowski et al. 2019). For further discussion on the observations of satellite planes, comparisons to cosmological simulations, and possible solutions to the problem, see Pawlowski (2018).

In light of the challenge that the VPOS poses to our theory of hierarchical structure formation, it is worthwhile to re-visit the analysis in Pawlowski et al. (2012) as our knowledge and understanding of the Milky Way’s substructures has evolved. In particular, there have been many newly discovered streams using high-

quality datasets, like those discovered in the Dark Energy Survey (Shipp et al. 2018) and in *Gaia* DR2 with the STREAMFINDER algorithm (Malhan et al. 2018; Ibata et al. 2019b). While some new streams have been analyzed in the context of the VPOS (Pawlowski & Kroupa 2014; Grillmair 2017a,b; Shipp et al. 2018), a consistent analysis of all recently discovered streams has been lacking to this point.

In addition, courtesy of *Gaia* DR2, we now have 6-D phase space measurements for nearly every Milky Way globular cluster (Gaia Collaboration et al. 2018b; Vasiliev 2019). This enables an assessment of VPOS membership for individual globular clusters, similar to the calculation performed in Fritz et al. (2018) for satellite galaxies, rather than analyzing the spatial distribution of the globular cluster system as a whole (Pawlowski et al. 2012; Arakelyan et al. 2018). If a significant fraction of individual globular clusters have orbital poles that align with the VPOS, it would strengthen the case for the VPOS even further.

It is not immediately clear if all of this new data confirms previous results from Pawlowski et al. (2012), strengthening the tension with Λ CDM, or possibly confuses the interpretation of the planes of satellites problem. To address this, we revisit the alignment of Milky Way stellar streams and globular clusters with the VPOS in light of recent discoveries and measurements. In particular, we calculate globular cluster orbital poles (Section 2) and stream normals (Section 3), evaluating the likelihood that they are members

of the VPOS while taking observational errors into account. We also employ orbit modeling (Section 4) in an attempt to associate Milky Way satellites with known streams. We discuss these results in the context of other recent studies in Section 5 and summarize our findings in Section 6.

2 GLOBULAR CLUSTERS

In this section, we analyze the globular cluster system of the Milky Way for preferential alignment of orbital poles with the VPOS normal. We divide the system into three populations according to their expected origin: old halo clusters that formed with the early Milky Way, young halo clusters that were accreted over time, and bulge/disk clusters that are confined to the Milky Way’s bulge and disk.

The accretion origin of the young halo clusters makes them particularly interesting in the context of the plane of satellites, as satellite galaxies also formed outside of the Milky Way and were accreted over time. If the young halo clusters have a similar spatial and kinematic distribution to the planar satellite galaxies, this would strengthen the case that the plane of satellites is both real and tied to the formation history of the Milky Way. Indeed, the young halo clusters have been found to have a flattened spatial distribution that aligns with the VPOS normal (Pawlowski et al. 2012; Arakelyan et al. 2018). Despite this finding, there has not been a detailed analysis of globular cluster orbital poles in the context of the VPOS.² We aim to rectify this situation here.

We use the classifications presented in Mackey & van den Bergh (2005) that are based on metallicity and horizontal-branch morphology index. This results in 70 old halo clusters, 30 young halo clusters, and 35 bulge/disk clusters, as well as 9 clusters that have been discovered more recently and were not classified in that work. We also analyze 6 clusters that were thought to be associated with the Sagittarius dwarf galaxy, though these are not our focus as Sagittarius’s orbital pole is almost perfectly misaligned with the VPOS normal.

2.1 Computing Galactocentric quantities

The 6-D phase-space information for each globular cluster is taken from the Vasiliev (2019) catalog of proper motions derived using data from *Gaia* Data Release 2 (Gaia Collaboration et al. 2018a). The catalog uses spatial information from Harris (1996) (2010 edition) and radial velocity measurements from Baumgardt et al. (2019). As in Vasiliev (2019), we assume an error of 0.1 in distance modulus for each cluster, corresponding to a relative error of 0.046 in the distance.

The orbital poles are computed relative to the center of the Milky Way as described in Pawlowski & Kroupa (2013). In summary, we convert each object’s heliocentric position, radial velocity, and proper motion into a Galactocentric Cartesian frame and calculate the angular momentum vector as the cross product of the position and velocity vectors. We then decompose this vector into a normalized direction (orbital pole). The orbital poles are reported in a spherical coordinate system (l_{MW}, b_{MW}) that is centered on

² Vasiliev (2019) briefly mentioned that the full system of globular cluster orbital poles does not appear to cluster with the VPOS normal. However, analyzing the globular clusters as one system mitigates any expected VPOS signal. For example, bulge/disk clusters are expected have orbital poles that tend to align with the Galactic poles, which are offset $\sim 90^\circ$ from the VPOS.

the Milky Way center and aligned with the standard heliocentric Galactic frame.

To estimate uncertainties, we perform 2,000 Monte Carlo simulations drawing from the uncertainties in the distance, radial velocity, and proper motions of each cluster. When drawing the proper motions, we account for the correlation between proper motions $\mu_{\alpha*} \equiv \mu_{\alpha} \cos \delta$ and μ_{δ} .

We assume a Galactocentric frame with a distance from the Sun to the Galactic centre of 8.122 kpc (Gravity Collaboration et al. 2018), a height of the Sun relative to the local Galactic mid-plane of 20.8 pc (Bennett & Bovy 2019), and a solar motion relative to the Galactic centre of $(v_x, v_y, v_z) = (12.9, 245.6, 7.78)$ km s⁻¹ (Drimmel & Poggio 2018, who combine exquisite measurements from Gravity Collaboration et al. 2018 and Reid & Brunthaler 2004), where the x -axis points from the position of the Sun projected on to the Galactic plane to the Galactic centre, the y -axis points towards Galactic longitude $l = 90^\circ$ (i.e. in the direction of Galactic rotation), and the z -axis points towards the North Galactic Pole. We note that, as for satellite galaxies (Metz et al. 2008; Pawlowski & Kroupa 2013), the orbital pole uncertainties for the globular clusters are dominated by uncertainties in the proper motion measurements. We therefore we refrain from incorporating the (small) uncertainties on Galactocentric frame properties in our analysis.

2.2 VPOS membership

Figure 2 shows the resulting distribution of globular cluster orbital poles, broken down by the different populations. The observed orbital pole (assuming no error in measurements) of each cluster is shown as a large circle and the uncertainty of the orbital pole is illustrated by the point clouds based on 2,000 Monte Carlo realizations. The green cross indicates the assumed VPOS normal of $(l_{MW}, b_{MW}) = (169.3^\circ, -2.8^\circ)$, as used to predict satellite galaxy proper motions in Pawlowski & Kroupa (2013) and evaluate their VPOS membership in Fritz et al. (2018). The green circles of opening angle $\theta_{inVPOS} = 36.87^\circ$ denote areas of 10% of the sphere around the VPOS normal. Orbital poles that lie within this region are considered to orbit along the VPOS (Fritz et al. 2018).

Based on the assumption that the cluster orbits along the VPOS, we can find the predicted orbital pole direction that best aligns with the VPOS based on spatial information alone. This is the direction along a great circle oriented perpendicular to the position of the cluster (as seen from the center of the Milky Way) which minimizes the angle to the assumed VPOS normal. With this optimal orbital pole, we can calculate the same summary statistics as in Fritz et al. (2018) to evaluate if a cluster is a member of the VPOS:

- θ_{pred} : the angle between the predicted orbital pole and the VPOS normal. If this exceeds θ_{inVPOS} , then VPOS membership is ruled out based on spatial information alone
- θ_{obs} : the angle between the observed orbital pole and the VPOS normal
- p_{inVPOS} : the fraction of Monte Carlo sampled orbital pole directions that fall within θ_{inVPOS} of the VPOS normal. This estimates the probability that a cluster is a VPOS member
- $p_{>VPOS}$: the fraction of Monte Carlo orbital pole directions that are further from the VPOS normal than θ_{inVPOS} after artificially rotating the Monte Carlo samples so that the observed pole falls on the predicted pole. This estimates the probability of falsely finding the cluster’s orbital pole to be misaligned with the VPOS
- $p_{>obs}$: the fraction of Monte Carlo orbital pole directions that are further from the VPOS normal than θ_{obs} after artificially ro-

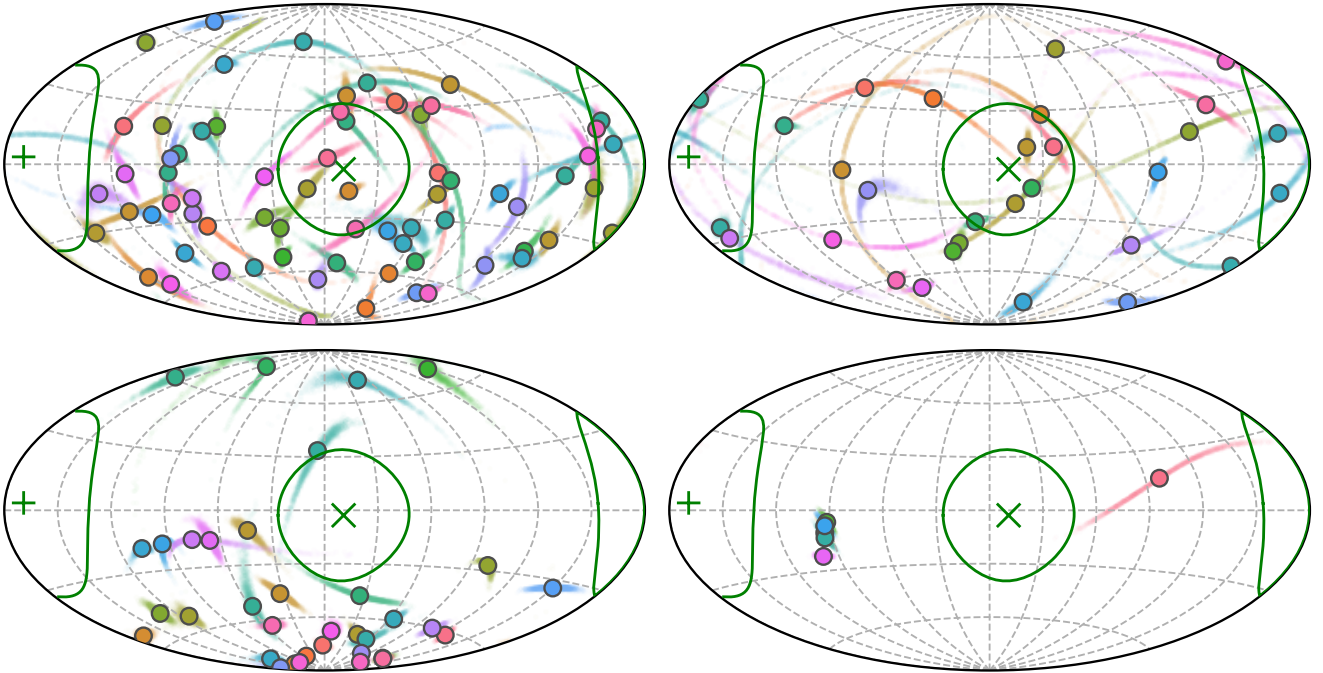


Figure 2. All-sky distribution of orbital poles for Milky Way globular clusters. The large points correspond to the observed (assuming no measurement errors) orbital poles, while the point clouds show the results of 2,000 Monte Carlo simulations incorporating measurement errors. The green circles each contain 10% of the sky around the assumed VPOS pole, given as an “x” for the co-orbiting direction and a “+” for the counter-orbiting direction. Each panel corresponds to a different population of globular clusters using the classifications from Mackey & van den Bergh (2005): old halo (top left), young halo (top right), bulge/disc (bottom left), and Sagittarius (bottom right). Only the young halo cluster population includes a substantial fraction of VPOS members ($\sim 30\%$, see Table 2).

tating the Monte Carlo samples so that the observed pole falls on the predicted pole. This estimates the probability of measuring an intrinsically well-aligned orbital pole as far away from the VPOS normal as observed. As this procedure assumes intrinsically aligned poles, this value should be considered a lower limit

A good candidate for VPOS membership would have $\theta_{\text{obs}} < \theta_{\text{inVPOS}}$, a large p_{inVPOS} , and a small $p_{>\text{VPOS}}$. We consider systems with $p_{\text{inVPOS}} > 0.5$ to be VPOS members, $p_{\text{inVPOS}} < 0.05$ to firmly and conclusively rule out VPOS membership, and intermediate values as too weakly constrained to be conclusive. This scheme is simple and reproduces most of the classifications that Fritz et al. (2018) arrived at for satellite galaxies (they do not state their classification criteria explicitly).

2.3 Results and comparison to isotropy

Table 1 provides an overview of the statistics used to determine VPOS membership. For the total population of Milky Way globular clusters, there is no obvious clumping of orbital poles within the confines of the VPOS; according to the criteria from Section 2.2, 19 clusters are VPOS members, 113 have well-constrained orbital poles that are misaligned with the VPOS, and 18 are not constrained enough to tell. These results are broadly consistent with Vasiliev (2019).

Separating the globular clusters by their suspected origin reveals a more interesting picture, as seen in the summary provided in Table 2 and illustrated in Figure 2. The most interesting population with respect to the VPOS is the young halo clusters. Pawlowski et al. (2012) found that the young halo clusters have a flattened

spatial distribution that is aligned with the Milky Way’s plane of satellite galaxies. We find that the orbital poles of young halo globular clusters are much more likely to align with the VPOS normal than those of other populations. Specifically, 9 of the 30 clusters have $p_{\text{inVPOS}} > 0.5$ and the sum of the membership probabilities (another way to estimate the number of VPOS members) for the young halo clusters is $\sum p_{\text{inVPOS}} = 9.82$.

It can be enlightening to compare this result to expectations from an isotropic distribution. The co-orbiting and counter-orbiting circles in Figure 2 each encompass 10% of the sky, so it would be reasonable to expect $\sim 20\%$ (in the case of young halo clusters, 6 of 30) of uniformly distributed poles to fall within this region. We can go further and calculate the probability that at least k out of n uniformly distributed orbital poles fall within the 10% circles on the sky. This is essentially a sum over Bernoulli experiments (see Pawlowski et al. 2012 for details):

$$P = \sum_{i=0}^{n-k} \binom{n}{k+i} p^{k+i} (1-p)^{n-k-i}, \quad (1)$$

where $p = 0.2$. The probability that at least $k = 9$ out of $n = 30$ poles fall within θ_{inVPOS} of the VPOS normal is 12.9% (for $k = 10$ this lowers to 6.1%). This is considerably higher than the results for satellite galaxies ($k = 19$ of $n = 41$ poles would fall within the VPOS tolerance 0.01% of the time).

In contrast, the orbital poles for old halo clusters do not show significant clumping in the direction of the VPOS normal. Of the 70 old halo clusters, 10 have $p_{\text{inVPOS}} > 0.5$ resulting in a $f_{\text{inVPOS}} = 0.143$, approximately half that of the young halo clusters. The sum of the membership probabilities for old halo clusters is $\sum p_{\text{inVPOS}} =$

Name	Type	l_{pole} [deg]	b_{pole} [deg]	Δ_{pole} [deg]	θ_{pred} [deg]	θ_{obs} [deg]	p_{inVPOS}	$p_{>\text{VPOS}}$	$p_{>\text{obs}}$
NGC 104	BD	52.5	-61.7	1.4	51.1	$-80.2^{+0.1}_{-0.1}$	0.000	0.000	0.000
NGC 288	OH	133.2	32.6	8.1	44.7	$49.2^{+4.2}_{-3.0}$	0.000	0.002	0.000
NGC 362	YH	143.7	9.6	15.7	27.0	$29.1^{+2.2}_{-0.9}$	0.946	0.040	0.065
Whiting 1	UN	284.1	-20.8	5.5	43.7	$-67.9^{+3.8}_{-3.4}$	0.000	0.000	0.000
NGC 1261	YH	265.2	39.7	17.2	21.6	$-79.4^{+7.2}_{-14.0}$	0.004	0.038	0.000

Table 1. Alignment with the VPOS for individual globular clusters (abridged version, see Table B1 for full list). ‘Type’ refers to the origin of the cluster (Mackey & van den Bergh 2005): old halo (OH), young halo (YH), bulge/disc (BD), Sagittarius (SG), and unclassified (UN). The orbital pole is reported in spherical coordinates ($l_{\text{MW}}, b_{\text{MW}}$) that are aligned with the heliocentric Galactic system and centered on the Milky Way center. Δ_{pole} is the angular uncertainty on the orbital pole direction, computed using the spherical standard distance. θ_{pred} is the minimum possible angle between the VPOS normal and the cluster’s orbital pole based on spatial information alone. θ_{obs} is the observed angle (positive value indicates co-orbiting with respect to the VPOS, negative for counter-orbiting). p_{inVPOS} is the probability that the cluster’s orbital pole aligns with the VPOS normal to within the 10% circle ($\theta_{\text{inVPOS}} = 36.87^\circ$). $p_{>\text{VPOS}}$ is the probability of falsely finding an intrinsically perfectly aligned orbital pole outside of this area given the measurement uncertainties. $p_{>\text{obs}}$ is the probability of finding an orbital pole at least as far inclined from the VPOS as the observed orbital pole. See Section 2.2 for details on these calculations. A likely VPOS member would have $\theta_{\text{obs}} < \theta_{\text{inVPOS}}$, a large p_{inVPOS} , and a small $p_{>\text{VPOS}}$.

Type	N	f_{inVPOS}	f_{notVPOS}	$f_{\text{inconclusive}}$	$\sum p_{\text{inVPOS}}/N$
OH	70	0.143	0.743	0.114	0.130
YH	30	0.300	0.467	0.233	0.327
BD	35	0.000	0.971	0.029	0.011
SG	6	0.000	1.000	0.000	0.005
UN	9	0.000	0.778	0.222	0.080
All	150	0.127	0.753	0.120	0.134
F18	41	0.463	0.293	0.244	0.437

Table 2. Summary of VPOS membership for each population of Milky Way globular clusters: old halo (OH), young halo (YH), bulge/disc (BD), Sagittarius (SG), and unclassified (UN). N is the total number of clusters for that population, f_{inVPOS} is the fraction of clusters with $p_{\text{inVPOS}} > 0.5$, f_{notVPOS} is the fraction of clusters with $p_{\text{inVPOS}} < 0.05$, $f_{\text{inconclusive}}$ is the remaining fraction of clusters for which VPOS membership is inconclusive (see Section 2.2 for details). The final column is the sum of the membership probabilities p_{inVPOS} for each population divided by the total number in that population; this is another way to estimate the fraction of VPOS members. We also include the results for satellite galaxies as classified by Fritz et al. (2018), with p_{inVPOS} values taken directly from their Table 4 (we add the LMC and SMC, assuming $p_{\text{inVPOS}} = 1$ for both). *The only globular cluster population with a substantial fraction of VPOS members is the young halo clusters, but the fraction of satellite galaxies that are VPOS members is considerably higher.*

9.12. The probability that at least $k = 10$ out of $n = 70$ uniformly distributed poles fall within the VPOS tolerance is 91.5%.

The bulge/disc clusters behave as expected, with orbital poles tending to fall near the co-orbiting pole of the Milky Way ($b_{\text{MW}} = -90^\circ$). Only one of the 35 bulge/disc clusters has non-negligible p_{inVPOS} (NGC 6440, with $p_{\text{inVPOS}} = 0.377$). These results are consistent with a population of globular clusters forming within the plane of the Milky Way disc (perpendicular to the VPOS normal).

The globular clusters associated with Sagittarius also behave as expected. Five of the clusters (NGC 6715, Terzan 7, Arp 2, Terzan 8, and Pal 12) have orbital poles that are well constrained and located near $(l_{\text{MW}}, b_{\text{MW}}) = (275.2, -8.0)$, the orbital pole of Sagittarius (Pawlowski & Kroupa 2020). Four of the five have $\theta_{\text{pred}} > \theta_{\text{inVPOS}}$; they are ruled out as VPOS members based on spatial information alone, as is the case with Sagittarius (they correspondingly have $p_{\text{inVPOS}} = 0$). The fifth cluster, Pal 12, has $\theta_{\text{pred}} = 3.34^\circ$ but also $p_{\text{inVPOS}} = 0$. The sixth cluster, NGC 4147, has an orbital pole that is not constrained well but actually nearly counter-orbits relative

to Sagittarius (its orbital pole point cloud is clearly offset from those of other Sagittarius clusters in the lower right panel of Figure 2). We discuss this cluster as it relates to Sagittarius in further detail in Section 5, but it is also ruled out as a VPOS member ($p_{\text{inVPOS}} = 0.023$).

3 STELLAR STREAMS

In this section, we analyze the stellar stream system of the Milky Way for preferential alignment with the VPOS normal. Stellar streams form as initially self-bound objects that fall into the Milky Way and are unraveled by the tidal forces of the Milky Way’s potential. This makes them extremely useful for tracing the hierarchical formation of the Milky Way (Peebles 1965; Press & Schechter 1974; Blumenthal et al. 1984).

An alignment of stellar streams with the Milky Way’s plane of satellite galaxies strengthens the case of the plane’s existence and expands its definition to include non-satellite objects as a Vast Polar Structure. Pawlowski et al. (2012) found that 7 of the 14 streams that had been discovered at the time aligned with the VPOS normal. This distribution of stream normals significantly deviates from an isotropic distribution (the probability of finding at least 7 of 14 isotropically-distributed normals within 32° of the VPOS normal is 0.24%).

Since that work, there have been several new streams discovered using either photometric surveys (e.g. Shipp et al. 2018) or kinematics from *Gaia* (e.g. Ibata et al. 2019b). In light of these discoveries, we re-examine the question of whether the distribution of stream normals remains preferentially aligned with the VPOS. To do this, we will calculate stream normals (§3.1) for every known Milky Way stream (§3.2) and analyze their alignment relative to the VPOS (§3.3).

3.1 Stream normal calculation

As in Pawlowski et al. (2012), we assume that stellar streams approximately trace the orbit of their progenitors (Odenkirchen et al. 2003). Specifically, we assume that the orbital plane of the stream can be approximated by the plane defined by two anchor points along the stream (most commonly the endpoints) and the Milky Way center. We note that just as the angular momentum vector is not an integral of motion and orbital poles effectively precess and nutate in a

non-spherical potential (Binney & Tremaine 2008), stream normals exhibit a similar behavior (Erkal et al. 2016). However, since VPOS membership is best defined as an aligned orbital pole to the VPOS normal (Fritz et al. 2018), we apply this same criteria using stream normals.

Once the two stream anchor points are determined (see §3.2), we can calculate the position of the stream normal. We begin by transforming the anchor points into Cartesian Galactocentric coordinates, assuming the same transformation as in Section 2.1. We then compute the normal of the plane as the normalized cross product of the two spatial anchor vectors. Proper motion information (and therefore the orbital direction) is not available for most streams, so the normals that we report are chosen to lie between $120^\circ < l_{\text{MW}} < 300^\circ$ to match Pawlowski et al. (2012).

To estimate uncertainties, we perform 2,000 Monte Carlo simulations drawing from the uncertainties in the angular positions and distances to each anchor point. When varying the angular positions, we displace the anchor point in a random direction on the sky by an angular offset drawn from a Gaussian with a mean of zero and a standard deviation given by the angular uncertainty as compiled in Table 3. The major source of uncertainty in the stream normal direction typically comes from distance uncertainties; these can be $\sim 20\%$ for streams discovered in photometric surveys using a matched-filter method (Shipp et al. 2018).

3.2 Assembling a catalog

We apply the method described above to 64 Milky Way streams that extend more than 4° along the sky. Our list of streams is based on the catalog in the `galstreams`³ package (Mateu et al. 2018) and augmented with more recent discoveries. We exclude shorter streams (Ophiucus; Bernard et al. 2014) and tidal deformations around some globular clusters (Eridanus and Pal 15; Myeong et al. 2017). We exclude cloud-like structures for which it is difficult to assign anchor points: EriPhe (Li et al. 2016), Hercules-Aquila, TriAnd1, TriAnd2, and the Virgo and Pisces Overdensities (Grillmair & Carlin 2016). We also exclude the Monoceros Ring due to its disputed nature as a stream or a feature of the Milky Way disk (Sheffield et al. 2018; Laporte et al. 2019). Additionally, we are forced to exclude the four streams (WG-1, WG-2, WG-3, WG-4) discovered in Agnello (2017) as they lack a distance measurement. The stream data are compiled in Table 3, along with respective references.

With no established convention for naming newly discovered streams, a “delightful anarchy” has ensued (Grillmair & Carlin 2016). Unfortunately, a similar anarchy has pervaded in how *properties of the streams* have been reported. Definitions of a stream footprint can include its endpoints, orbital pole, midpoint along the stream, or simply the coordinates of individual stars believed to be stream members. The width of the streams, fit along a coordinate perpendicular to the stream, can be reported as the standard deviation of a Gaussian or as a full-width at half-maximum (FWHM) of the stellar density. Further complications arise when studies provide these quantities in Galactocentric coordinates, sometimes without stating the assumptions required to transform from observed heliocentric coordinates.

In an attempt to wrangle this situation, we provide stream anchor points in a consistent format. For each stream, we provide heliocentric on-sky positions of the anchor points, heliocentric distances to the anchors, and the Gaussian width of the stream per-

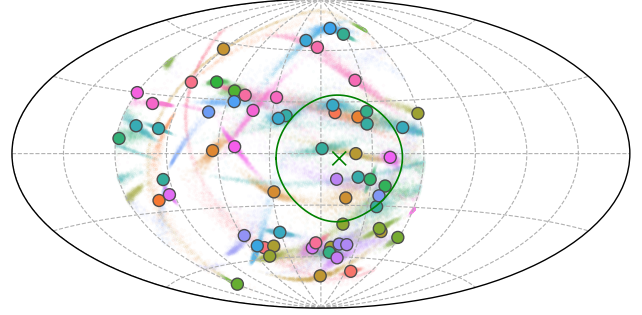


Figure 3. All-sky distribution of normals for Milky Way streams. Only one of the two normals (those from $120^\circ < l_{\text{MW}} < 300^\circ$) are shown. The large points correspond to the observed (assuming no measurement errors) normals, while the point clouds show the results of 2,000 Monte Carlo simulations incorporating measurement errors. The green circle contains 10% of the sky around the assumed VPOS normal (marked as an “x”). *The Milky Way streams do not appear to preferentially align with the VPOS normal.*

pendicular to the stream track. If a stream width was reported as a FWHM in the reference, we convert this to a Gaussian standard deviation assuming the FWHM corresponds to that of a Gaussian (FWHM = 2.355σ).

When compiling this catalog, three classes of references emerged. Streams classified as Class 1 have references that report each of these quantities explicitly, allowing us to simply copy the values into our catalog with no extra work. Typically we either adopt the width of the stream or the precision to which the endpoint is reported for the angular uncertainty on the endpoint $\Delta\theta$, whichever is the larger of the two.

Streams classified as Class 2 have references that provide distance measurements and widths explicitly, but do not explicitly provide endpoints. In this case, we use the endpoints computed using `galstreams` and confirm that these match with figures of the stream in the reference. As these endpoints are derived from representations of the stream, we assume an uncertainty on the endpoint position of $\Delta\theta = 0.5^\circ$ regardless of stream width. Out of the 64 streams analyzed, 31 fall under Class 1 and 14 fall under Class 2.

Eighteen of the remaining streams required additional analysis to obtain anchor points. For many of these, the endpoints computed by `galstreams` did not match the ends of the `galstreams` footprint and needed to be identified separately. Others use overdensities along the stream (e.g. the PAndAS stream) or globular clusters the stream originates from (e.g. the NGC 5466 stream) rather than a poorly-resolved endpoint for the anchor. Each of these cases is described in detail in Appendix A.

Finally, the Sagittarius stream has multiple wraps around the Milky Way and is not well described by two anchor points, but its orbital plane has been studied in detail (Majewski et al. 2003; Fellhauer et al. 2006). We simply adopt the normal reported by Law & Majewski (2010) of $(l_{\text{MW}}, b_{\text{MW}}) = (273.8, -14.5)$. We include the Sagittarius stream in the results quoted below and assume it has $p_{\text{inVPOS}} = 0$.

3.3 Results and comparison to isotropy

Figure 3 shows the on-sky distribution of Milky Way stream normals. The figure includes the direction of the assumed VPOS normal $(l_{\text{MW}}, b_{\text{MW}}) = (169.3^\circ, -2.8^\circ)$ and the angular tolerance

³ <https://github.com/cmateur/galstreams>

Name	Class	RA [deg]	Dec [deg]	Distance [kpc]	$\Delta\theta$ [deg]	Length [deg]	Width [deg]	l_{normal} [deg]	b_{normal} [deg]	θ_{obs} [deg]	p_{inVPOS}	Ref.
20.0-1	3	112.92	61.56	12.6 ± 1.3	1.8	158.6	1.8	270.2	38.0	$76.4^{+8.3}_{-6.0}$	0.000	Mateu et al. (2018)
Acheron	1	273.92	-43.35	28.1 ± 2.8	1.8							
		230.00	-2.00	3.8 ± 0.8	0.5	36.5	0.4	228.2	-53.6	$70.4^{+6.9}_{-5.1}$	0.000	Grillmair (2009)
ACS	1	126.40	-0.70	8.9 ± 0.2	2.1	65.1	2.1	143.5	-68.0	$67.5^{+0.4}_{-0.4}$	0.000	Grillmair (2006)
		133.90	64.20	8.9 ± 0.2	2.1							
Aliqa Uma	1	31.70	-31.50	28.8 ± 5.8	0.3	10.0	0.3	171.3	23.8	$29.9^{+13.5}_{-5.3}$	0.717	Shipp et al. (2018)
		40.60	-38.30	28.8 ± 5.8	0.3							

Table 3. The list of streams analyzed in this work (abridged version, see Table B4 for full list). For each stream, we compile two anchor points (usually the two endpoints of the stream) and provide their position on the sky, heliocentric distance, and angular uncertainty $\Delta\theta$. We also calculate the stream length (on-sky angular separation between the two anchor points) and provide the stream width (Gaussian σ perpendicular to the stream) reported in the reference. The stream normal is reported in spherical coordinates ($l_{\text{MW}}, b_{\text{MW}}$) that are aligned with the heliocentric Galactic system and centered on the Milky Way center. The angular distance of the stream normal from the VPOS normal is θ_{obs} and the fraction of Monte Carlo stream normals that fall within the 10% circle centered on the VPOS normal is p_{inVPOS} .

$\theta_{\text{inVPOS}} = 36.87^\circ$ around that direction. Although the normal vectors are two-directional, since we do not know the orbital sense only one direction is plotted. To match the range used in Pawlowski et al. (2012) for easy comparison, only normals within $120^\circ < l_{\text{MW}} < 300^\circ$ are plotted.

For each stream, we calculate the angular distance θ_{obs} of the Monte Carlo stream normals from the VPOS normal and the fraction p_{inVPOS} of Monte Carlo normals that fall within θ_{inVPOS} of the VPOS normal. These quantities are presented in Table 3.

Overall, we do not find a tendency for stream normals to be clustered in the direction of the VPOS normal. Of the 64 streams, 39 are excluded from VPOS membership ($p_{\text{inVPOS}} < 0.05$) and only 12 are likely VPOS members ($p_{\text{inVPOS}} > 0.5$). The sum of membership probabilities for all streams is $\sum p_{\text{inVPOS}} = 13.32$. The probability that at least $k = 12$ out of $n = 64$ uniformly distributed normals fall within the VPOS tolerance is 64.8% (for $k = 14$ this lowers to 40.2%).

The cumulative distribution of angular distances θ_{obs} between stream normals and the VPOS normal is plotted in Figure 4. The shaded bands correspond to the 1- and 2- σ confidence intervals as a result of the Monte Carlo simulations. We also show results using the stream catalog from Pawlowski et al. (2012) for comparison. Adding in new stream discoveries has alleviated the difference between the observed stream normal distribution and an isotropic distribution (black dashed line).

Finally, it is possible that our position as observers leads us to over-represent streams that are not aligned with the VPOS. Due to geometric effects, a stream defined by anchor points with heliocentric distance d_\odot smaller than the distance between the Sun and the Galactic center d_{GC} cannot lead to stream normals closer to $(l_{\text{MW}}, b_{\text{MW}}) = (180, 0)^\circ$ or $(0, 0)^\circ$ than

$$\tan \alpha = \sqrt{\left(\frac{d_\odot}{d_{\text{GC}}}\right)^2 - 1}. \quad (2)$$

Since the VPOS normal is close to $(180, 0)^\circ$, streams that are close to the Sun (and thus easier to observe) might bias the overall sample against VPOS membership (Pawlowski et al. 2012).

However, our results remain substantively unchanged after taking this effect into account. When excluding all streams in the sample that have an anchor point with $d_\odot = 8.122$ kpc (15 streams with $p_{\text{inVPOS}} \approx 0$), 24 of the remaining 49 streams have $p_{\text{inVPOS}} < 0.05$, 12 have $p_{\text{inVPOS}} > 0.5$, and $\sum p_{\text{inVPOS}} = 13.30$. The probability that at least $k = 12$ out of $n = 49$ uniformly distributed normals

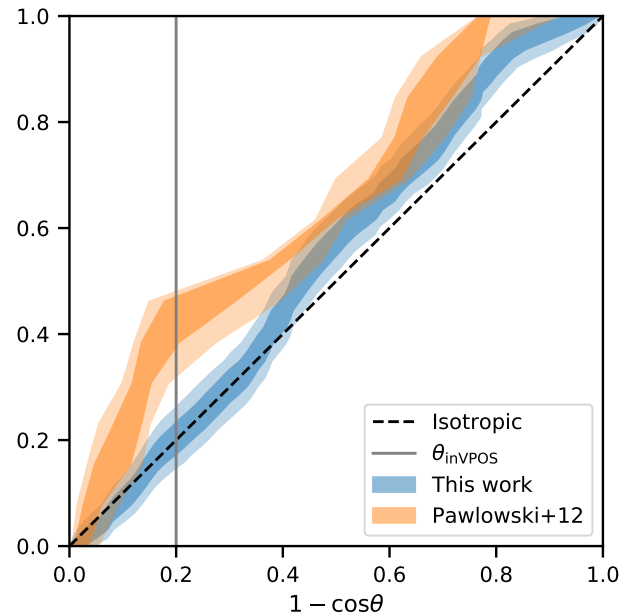


Figure 4. Cumulative distribution of stream normals within a fraction of half-sphere measured from the VPOS normal. We show the distribution of normals for streams used in this work (blue), the distribution of normals for the data compiled in Pawlowski et al. (2012) (orange), the expectation for an isotropic distribution (black dashed), and the angular tolerance from the VPOS normal to be considered a member (grey solid). Shaded bands correspond to the 1- and 2- σ confidence intervals from Monte Carlo simulations. Our current census of stellar streams indicates no preferential alignment with the VPOS normal.

fall within the VPOS tolerance is 26.5% (for $k = 14$ this lowers to 9.7%). It does not appear that this projection effect (in conjunction with many newly discovered streams being nearby) can explain the shift in the inferred distribution of stream normals with respect to the VPOS.

3.4 Comparison to prior studies

While some streams discovered since 2012 have been analyzed in the context of the VPOS, it has largely been a patchwork of techniques

that are only applied to streams whose discoveries were announced in those studies. Here, we compare our results for the alignment of individual streams with the VPOS to those from other studies.

Our results and those from prior studies that explicitly focus on the VPOS (Pawlowski et al. 2012, 2015a) agree very well. We find that most streams already classified as VPOS members (ATLAS, Cocytos, the Magellanic Stream, Pal 5, and Styx) all have $p_{\text{inVPOS}} \gtrsim 0.9$. The two exceptions are Lethe and the NGC 5053 stream, which have normals located near the edge of the boundary for VPOS consideration, resulting in $p_{\text{inVPOS}} = 0.48$ even though they been classified as VPOS members. The streams already classified as non-members (ACS, Acheron, Cetus, GD-1, NGC 5466, Orphan, PAndAS, Sagittarius, Triangulum/Pisces) all have $p_{\text{inVPOS}} = 0$. We excluded the GCN stream (Jin 2010) due to its tentative nature, though it is worth noting that it has been classified as a VPOS member.

Some studies have attempted to use orbit modeling to associate discovered streams with the VPOS, constraining the orbit using distances and stream tracks along the sky. Using this method, Grillmair (2017a) found that PS1-D, Sangarius, and Scamander align with the VPOS and Grillmair (2017b) found that Molonglo and Murrumbidgee align with the VPOS while Kwando and Orinoco do not. Strangely, we find nearly the opposite results: PS1-D, Sangarius, and Scamander all have $p_{\text{inVPOS}} = 0$, while Kwando, Molonglo, Murrumbidgee, and Orinoco have $p_{\text{inVPOS}} = 0.54, 0.53, 0.16,$ and 0.27 , respectively. This discrepancy merits further investigation, but may possibly be due to the potential assumed for the calculation (Allen & Santillan 1991).

Shipp et al. (2018) performed a search for stellar streams in the Dark Energy Survey, recovering four previously known streams and discovering 11 new ones. They employed a very similar Monte Carlo technique as presented here to calculate stream normals (their Figure 17) and concluded that their stream sample did not preferentially align with the VPOS, without commenting on any individual streams that could be members. However, their analysis did not account for the unknown orbital sense (such that a stream normal could be further than 90° from the VPOS normal) and effectively assumed the VPOS to have zero thickness ($\theta_{\text{inVPOS}} \approx 0^\circ$). Using their stream endpoint data, we find that 6 of the 15 streams in the DES footprint have $p_{\text{inVPOS}} > 0.5$ (ATLAS, Aliqa Uma, Elqui, Indus, Molonglo, and Ravi) and that $\sum p_{\text{inVPOS}} = 5.61$ for the entire sample.

Finally, some studies have analyzed cloud-like structures in the context of the VPOS. Li et al. (2016) discovered the EriPhe overdensity and noted that EriPhe, Hercules-Aquila, and the Virgo Overdensity fall along a polar great circle nearly aligned with the VPOS, suggesting that all three structures are remnants left by a single dwarf galaxy that was a VPOS member. Boubert et al. (2019) used *Gaia* RR Lyrae to characterize the Virgo Overdensity and noted the overdensity as aligning with the Magellanic Stream and the VPOS. We excluded these cloud-like structures from our analysis because it is difficult to assign anchor points to such large, complex structures.

3.5 Other clustering of stream normals

While there is no clustering of stream normals in the VPOS direction, there does appear to be a cluster of normals in Figure 3 near $(l_{\text{MW}}, b_{\text{MW}}) = (180, -60)^\circ$. Repeating the same calculations for this new direction confirms the clustering, with 11 streams (ACS, EBS, Fimbulthul, Fjörm, Gaia-3, Kshir, Orphan, PS1-D, Sangarius, Scamander, Ylgr) having $p_{\text{in-cluster}} \approx 1$ and the total

$\sum p_{\text{in-cluster}} = 19.75$. The probability that at least $k = 19$ out of $n = 64$ uniformly distributed normals fall within the assumed tolerance is 4.2%. The orbital poles for the young halo globular clusters are not concentrated in this direction.

There are several caveats to keep in mind regarding this apparent clustering. Some of the streams have been claimed as a features/warps in the Milky Way’s stellar disk (ACS, EBS) rather than the remnants of an accretion event (Deason et al. 2018; Laporte et al. 2019). Several others are thought to be associated with each other (GD-1 and Kshir; Malhan et al. 2019) or overlap in observed space such that an association is possible (Orphan, PS1-D, Sangarius, and Scamander; Grillmair 2017a). Removing even some of these streams from the catalog would alleviate the discrepancy from an isotropic distribution. Finally, it is difficult to quantify the significance of this clustering without a handle on the selection function for detecting stellar streams and how that selection function projects onto orbital plane space. Future spectroscopic confirmation of stream candidates and in-depth studies of this selection function will help to determine if this clustering of stream normals is significant.

4 ORBIT MODELING

While we have shown that Milky Way streams and globular clusters as *systems* are not associated with the plane of satellites, it can still be interesting to associate *individual* objects that are VPOS members to attempt to establish a common origin (e.g. group infall). Independently of the VPOS, associating streams with known objects can point towards the progenitor of the stream and trace the process of hierarchical formation. In this section, we integrate orbits for all of the Milky Way satellites (dwarf galaxies and globular clusters) to attempt to associate them with observed stellar streams.

4.1 Methodology

The full modelling of a satellite being unraveled into a stellar stream is challenging, as the results depend on the shape of the Galactic potential, internal and orbital kinematics of the progenitor, and the effects of dynamical friction and time-dependent substructures like the Galactic bar and the LMC. For simplicity, and due to the fact that we have limited information of each stream (the two anchor points), we integrate orbits in static potentials that do not include the effects Galactic substructures or the LMC.

To associate a satellite with a stream, we integrate the satellite’s orbit backwards in time for 1 Gyr using *gal*a (Price-Whelan 2017). For each object and stream pairing, we check if the orbit passes through the on-sky position of the stream’s anchor points at approximately the right heliocentric distance. If an orbit passes through both stream anchor points, within the corresponding $1-\sigma$ angular and distance uncertainties (see Table 3), then it is considered an association.

Our initial conditions for the orbits of the globular clusters are the same as in Section 2. For the satellite galaxies, we use the compilation of position and velocity observations in Table A1 of Riley et al. (2019).⁴ We perform 2,000 Monte Carlo simulations of these initial conditions by sampling over uncertainties in the distance, radial velocity, and proper motions of each satellite. By

⁴ We adopt the proper motion measurements from Fritz et al. (2018) except for the Magellanic Clouds, for which we use measurements from Gaia Collaboration et al. (2018b).

	ω Cen Fimbulthul	NGC 3201 Gjöll	NGC 4590 PS1-E
Price-Whelan (2017)	0.000	0.577	0.012
Bovy (2015)	0.189	0.271	0.141
Law & Majewski (2010)	0.035	0.398	0.000

Table 4. Potential associations between Milky Way satellites and known stellar streams based on orbit modeling. Results are presented as the fraction of Monte Carlo orbit integrations that pass through both stream endpoints (see Section 4 for details). Orbits are integrated in three different potentials (Price-Whelan 2017; Bovy 2015; Law & Majewski 2010). We recover the previously known association between ω Cen and Fimbulthul (Ibata et al. 2019a), as well as a new possible association between NGC 3201 and Gjöll.

counting the fraction of Monte Carlo orbits for each satellite-stream pairing that are “associated,” we get a sense of which pairings are possible given the measurement uncertainties.

We repeat this procedure for three different Milky Way potentials that are implemented in *gal*: the Milky Way mass model in Price-Whelan (2017), `MWPotential2014` as described in Bovy (2015), and the potential used by Law & Majewski (2010). Each of these potentials uses some combination of component potentials used to represent the dark matter halo and (static) Galactic baryonic structures. In practice, these potentials vary the total mass and mass distributions while still being reasonably consistent with the latest constraints, allowing us to probe the effects of changing the potential on satellite-stream pairings.

4.2 Results and the NGC 3201 – Gjöll connection

The main results of this procedure are shown in Table 4. We find only three satellite-stream pairings that were associated in 5% or more of the 2,000 Monte Carlo simulations for *any* of the 3 potentials. One of these is the previously reported association between ω Cen (NGC 5139) and the Fimbulthul stream (Ibata et al. 2019a). Of the three possible associations in Table 4, all have $p_{\text{inVPOS}} = 0$.

Independently of the VPOS, we want to draw attention to the possible association between NGC 3201 and the Gjöll stellar stream. This pairing had a high fraction of Monte Carlo orbit integrations pass through the stream relative to other pairings, independent of which Milky Way potential was adopted. The cluster and the stream are also very close to each other; one only needs to integrate NGC 3201’s orbit backwards ~ 25 Myr to overlap with the stream.

NGC 3201 is a young halo cluster (Mackey & van den Bergh 2005) with a retrograde and eccentric orbit (Gaia Collaboration et al. 2018b). The best-fit orbit of the Gjöll stream from Ibata et al. (2019b) lies in a similar parameter space as NGC 3201 in $E - L_z$ (our orbit integration results can be considered a natural manifestation of this fact). Noting this similarity, Bianchini et al. (2019) used *Gaia* DR2 data to identify tidal tails coming off of the cluster. Taken together, these results suggest that NGC 3201 experienced tidal stripping that formed into the Gjöll stream. Combining *Gaia* DR2 kinematics with independent elemental abundances to chemo-dynamically tag Gjöll stars as NGC 3201 members would further link these two structures (Hansen et al. 2020, in preparation).

5 DISCUSSION

We have shown that the distributions of Milky Way globular cluster orbital poles (Section 2) and stellar stream normals (Section 3) are not significantly clustered in the direction of the VPOS normal. It

can be tempting to use these results to reject the notion of a plane of satellites problem altogether. However, we strongly caution against this.

The classical satellite galaxies of the Milky Way have been shown to have a highly-clustered distribution of orbital poles (Pawlowski & Kroupa 2013), a trend that has become more significant as higher-precision proper motion measurements become available (Pawlowski & Kroupa 2020) and that extends to Milky Way ultrafaint satellites (Fritz et al. 2018). This observed clustering of satellite orbital poles is not consistent with expectations from cosmological simulations, regardless of whether the simulations considered are dark-matter-only (Pawlowski & McGaugh 2014; Pawlowski et al. 2014; Ibata et al. 2014b) or include baryonic effects (Müller et al. 2018; Pawlowski et al. 2019). There is also considerable evidence for rotationally-supported planes in other satellite systems within the Local Group, namely around M31 (Ibata et al. 2013; Santos-Santos et al. 2019) and Centaurus A (Müller et al. 2018). Taking this observed plane of satellite galaxies as given, we have to consider why other accreted material—young halo globular clusters and stellar streams—*doesn’t* exhibit the same behavior.

The first possibility is that the plane of satellite galaxies represents a particularly stable orbital configuration and that the accreted clusters and streams are from progenitors that happened on easily consumed orbital trajectories. The underlying physical reason could be related to the host (e.g. the orientation of the disk), intrinsic properties of the progenitors (e.g. less dense), or the orbits of the progenitors (e.g. closer pericenters) that have somehow resulted in polar orbits being longer-lived. This explanation can be tempting, as Sagittarius is in the process of disrupting and its orbital pole is located the furthest from the VPOS normal of any classical satellite (Pawlowski & Kroupa 2020). However, this mechanism would lead to a *dearth* of orbital poles in the direction of the VPOS normal, rather than the observed distribution that is reasonably consistent with isotropy (see Figure 4). Furthermore, satellite planes initialized in controlled simulations with static potentials disintegrate fairly rapidly (within 1-4 Gyr) due to subhalo-subhalo interactions, any asphericity of the potential, and deviations from a polar orientation (Fernando et al. 2017, 2018).

The second possibility is that there is no “safe” orbital configuration and that the Milky Way’s (stable) plane of satellites has formed recently, likely as a result of group infall. This formulation agrees with the observed, nearly isotropic distribution of accreted material and opens the door to attributing many VPOS members to, for example, the LMC coming in on its first infall (Besla et al. 2007). However, using inferred infall times from comparing *Gaia* kinematics to subhalos in cosmological simulations (Fillingham et al. 2019), high-probability VPOS satellite galaxy members have a range of infall times approximately 7-10 Gyr ago. This is much longer than the 1-4 Gyr lifespan of satellite planes in controlled simulations, making the scenario of a recent group infall unlikely. Additionally, detailed orbit integrations of 20 satellite galaxies (most of which are VPOS members) in a joint Milky Way, LMC, and SMC potential find that only half can be attributed to the LMC/SMC system (Patel et al. 2020).

We also re-iterate that the orbital planes of globular clusters and streams effectively precess and nutate with time (Binney & Tremaine 2008; Erkal et al. 2016). While modeling this process is subject to assumptions about the progenitor’s orbit and properties of the host halo, including its total mass and triaxiality, Erkal et al. (2016) quantified the orbital evolution of streams in aspherical potentials and found the precession rate for polar orbits to be $\sim 10^\circ \text{ yr}^{-1}$. Importantly for our results, they suggest that orbital

planes aligned with the polar axis are the shortest-lived. More detailed simulations of stream evolution, including examples in triaxial potentials, are warranted to see if the observed distribution of stream normals is consistent with theoretical expectations.

The association of stellar streams with the VPOS is further complicated by the gravitational presence of the LMC. The LMC is a massive satellite that has been shown to perturb streams in the Southern Hemisphere, displacing a stream's systemic proper motion from its track on the sky (Erkal et al. 2019; Shipp et al. 2019). Depending on the size of the offset (which has been observed to vary based on sky position, distance from the LMC, and stream width), this effect can make the stream normal computed using the two-anchor-point method a less reliable indicator of the orbital plane. Detailed modeling of this effect in the context of the VPOS will require radial velocities for member stars of the affected streams, something that may be possible with upcoming data releases from the S^5 survey (Li et al. 2019).

Finally, it is worth commenting on NGC 4147's relation to the Sagittarius dwarf galaxy. NGC 4147 is classified as a Sagittarius globular cluster by Mackey & van den Bergh (2005), however it is currently counter-orbiting with respect to Sagittarius (see Figure 2, lower right panel) while the other 5 Sagittarius clusters (NGC 6715, Terzan 7, Arp 2, Terzan 8, and Pal 12) have orbital poles that clump near Sagittarius's pole (Vasiliev 2019). This confirms prior results based on HST proper motions (Sohn et al. 2018) and agrees with spectroscopic abundance measurements (Villanova et al. 2016) that suggest that the cluster is not associated with Sagittarius, but rather could be from *Gaia*-Enceladus (Massari et al. 2019).

6 SUMMARY

In this work we have analyzed Milky Way globular clusters and stellar streams for dynamical alignment with the Milky Way's plane of satellites. After computing globular cluster orbital poles and stream normals, we determine VPOS membership for each cluster and stream using Monte Carlo simulations to take observational uncertainties into account. We compare the resulting distributions of orbital poles and stream normals to those expected from an isotropic distribution. Finally, we use an orbit modeling scheme to attempt to associate Milky Way satellites with known stellar streams. A summary of our main results is as follows:

- Utilizing the latest globular cluster proper motions inferred from *Gaia* DR2 data, we find that globular cluster orbital poles are not clustered in the VPOS direction. The young halo clusters, the population expected to be associated with the VPOS, have the highest fraction of VPOS membership ($\sim 30\%$), but this is substantially lower than the fraction of satellite galaxies associated with the VPOS. If the orbital poles were drawn from a uniform distribution, such an alignment around the VPOS would occur in at most 12.9% of cases, much higher than the $\sim 0.1\%$ typically quoted in VPOS studies (Pawlowski et al. 2012).

- Using our compilation of stream anchor points in Table 3, we similarly find that stellar stream normals are not clustered around the VPOS normal. Of the 64 streams analyzed here, 12 of them align with the VPOS; drawing from a uniform distribution results in similar clustering up to 64.8% of the time. Streams discovered since prior analysis in Pawlowski et al. (2012) have shifted the observed distribution of stream normals away from being clustered in the VPOS direction (Figure 4). These results are not substantially impacted by geometric effects due to our position as observers.

- Through our orbit modeling procedure, we find three possible instances of Milky Way globular clusters being associated with stellar streams. None of these pairings are of members of the VPOS, making orbit modeling an unlikely avenue for studying the VPOS as a consequence of hierarchical structure formation.

- Based on our orbit modeling, it is quite likely that globular cluster NGC 3201 is connected to the Gjöll stream. Information from chemical abundances and radial velocity measurements of stream stars could confirm this association (Hansen et al. 2020, in preparation).

- It is very unlikely that NGC 4147 is a Sagittarius globular cluster, based on the fact that it is nearly counter-orbiting with respect to Sagittarius (Figure 2, lower right panel).

Finally, we echo our caution against using our results to reject the notion of the plane of satellites problem. The satellite galaxies of the Milky Way have been shown to have a highly-clustered distribution of orbital poles (Fritz et al. 2018; Pawlowski & Kroupa 2020), an observation that is not consistent with expectations from Λ CDM (Pawlowski et al. 2019). However, our results do counter the notion that the Milky Way's plane of satellites is part of a pronounced Vast Polar Structure comprised of satellite galaxies, globular clusters, and stellar streams. Our hope is that these results raise interesting questions about the stability of planar configurations and may guide future studies on satellite planes in the context of hierarchical structure formation.

ACKNOWLEDGEMENTS

We thank Peter Ferguson, Davide Massari, Andrew Pace, and Marcel Pawlowski for their helpful comments, as well as an anonymous referee for their thoughtful reading. AHR acknowledges support from a Texas A&M University Merit Fellowship and an NSF Graduate Research Fellowship through Grant DGE-1746932. LES acknowledges support from DOE Grant No. de-sc0010813. This research made use of the Python Programming Language, along with many community-developed or maintained software packages including Astropy (Astropy Collaboration et al. 2013, 2018), gala (Price-Whelan 2017; Price-Whelan et al. 2017), Jupyter (Kluyver et al. 2016), Matplotlib (Hunter 2007), NumPy (van der Walt et al. 2011), Pandas (McKinney 2010), SciPy (Jones et al. 2001), and Seaborn (seaborn.pydata.org). This research made extensive use of arXiv.org and NASA's Astrophysics Data System for bibliographic information.

REFERENCES

- Agnello A., 2017, *MNRAS*, **471**, 2013
 Ahmed S. H., Brooks A. M., Christensen C. R., 2017, *MNRAS*, **466**, 3119
 Allen C., Santillan A., 1991, *Rev. Mex. Astron. Astrofis.*, **22**, 255
 Arakelyan N. R., Pilipenko S. V., Libeskind N. I., 2018, *MNRAS*, **481**, 918
 Astropy Collaboration et al., 2013, *A&A*, **558**, A33
 Astropy Collaboration et al., 2018, *AJ*, **156**, 123
 Baumgardt H., Hilker M., Sollima A., Bellini A., 2019, *MNRAS*, **482**, 5138
 Bennett M., Bovy J., 2019, *MNRAS*, **482**, 1417
 Bernard E. J., et al., 2014, *MNRAS*, **443**, L84
 Bernard E. J., et al., 2016, *MNRAS*, **463**, 1759
 Besla G., Kallivayalil N., Hernquist L., Robertson B., Cox T. J., van der Marel R. P., Alcock C., 2007, *ApJ*, **668**, 949
 Bianchini P., Ibata R., Famaey B., 2019, *ApJ*, **887**, L12
 Binney J., Tremaine S., 2008, *Galactic Dynamics: Second Edition*. Princeton University Press

- Blumenthal G. R., Faber S. M., Primack J. R., Rees M. J., 1984, *Nature*, **311**, 517
- Bonaca A., Geha M., Kallivayalil N., 2012, *ApJ*, **760**, L6
- Boubert D., Belokurov V., Erkal D., Iorio G., 2019, *MNRAS*, **482**, 4562
- Bovy J., 2015, *ApJS*, **216**, 29
- Brüns C., et al., 2005, *A&A*, **432**, 45
- Buck T., Macciò A. V., Dutton A. A., 2015, *ApJ*, **809**, 49
- Bullock J. S., Boylan-Kolchin M., 2017, *ARA&A*, **55**, 343
- Cautun M., Wang W., Frenk C. S., Sawala T., 2015a, *MNRAS*, **449**, 2576
- Cautun M., Bose S., Frenk C. S., Guo Q., Han J., Hellwing W. A., Sawala T., Wang W., 2015b, *MNRAS*, **452**, 3838
- Conn A. R., et al., 2013, *ApJ*, **766**, L20
- D’Onghia E., Lake G., 2008, *ApJ*, **686**, L61
- Deason A. J., et al., 2014, *MNRAS*, **444**, 3975
- Deason A. J., Belokurov V., Koposov S. E., 2018, *MNRAS*, **473**, 2428
- Drake A. J., et al., 2013a, *ApJ*, **763**, 32
- Drake A. J., et al., 2013b, *ApJ*, **765**, 154
- Drimmel R., Poggio E., 2018, *Research Notes of the American Astronomical Society*, **2**, 210
- Erkal D., Sanders J. L., Belokurov V., 2016, *MNRAS*, **461**, 1590
- Erkal D., et al., 2019, *MNRAS*, **487**, 2685
- Fellhauer M., et al., 2006, *ApJ*, **651**, 167
- Fernando N., Arias V., Guglielmo M., Lewis G. F., Ibata R. A., Power C., 2017, *MNRAS*, **465**, 641
- Fernando N., Arias V., Lewis G. F., Ibata R. A., Power C., 2018, *MNRAS*, **473**, 2212
- Fillingham S. P., et al., 2019, arXiv e-prints, p. [arXiv:1906.04180](https://arxiv.org/abs/1906.04180)
- Fritz T. K., Battaglia G., Pawlowski M. S., Kallivayalil N., van der Marel R., Sohn S. T., Brook C., Besla G., 2018, *A&A*, **619**, A103
- Gaia Collaboration et al., 2018a, *A&A*, **616**, A1
- Gaia Collaboration et al., 2018b, *A&A*, **616**, A12
- Gravity Collaboration et al., 2018, *A&A*, **615**, L15
- Grillmair C. J., 2006, *ApJ*, **651**, L29
- Grillmair C. J., 2009, *ApJ*, **693**, 1118
- Grillmair C. J., 2011, *ApJ*, **738**, 98
- Grillmair C. J., 2014, *ApJ*, **790**, L10
- Grillmair C. J., 2017a, *ApJ*, **834**, 98
- Grillmair C. J., 2017b, *ApJ*, **847**, 119
- Grillmair C. J., 2019, *ApJ*, **884**, 174
- Grillmair C. J., Carlin J. L., 2016, *Stellar Streams and Clouds in the Galactic Halo*. Springer International Publishing, p. 87, doi:10.1007/978-3-319-19336-6_4
- Grillmair C. J., Dionatos O., 2006, *ApJ*, **641**, L37
- Grillmair C. J., Johnson R., 2006, *ApJ*, **639**, L17
- Grillmair C. J., Cutri R., Masci F. J., Conrow T., Sesar B., Eisenhardt P. R. M., Wright E. L., 2013, *ApJ*, **769**, L23
- Harris W. E., 1996, *AJ*, **112**, 1487
- Hunter J. D., 2007, *Computing In Science & Engineering*, **9**, 90
- Ibata R. A., et al., 2013, *Nature*, **493**, 62
- Ibata N. G., Ibata R. A., Famaey B., Lewis G. F., 2014a, *Nature*, **511**, 563
- Ibata R. A., Ibata N. G., Lewis G. F., Martin N. F., Conn A., Elahi P., Arias V., Fernando N., 2014b, *ApJ*, **784**, L6
- Ibata R. A., Famaey B., Lewis G. F., Ibata N. G., Martin N., 2015, *ApJ*, **805**, 67
- Ibata R. A., Malhan K., Martin N. F., Starkenburg E., 2018, *ApJ*, **865**, 85
- Ibata R. A., Bellazzini M., Malhan K., Martin N., Bianchini P., 2019a, *Nature Astronomy*, **3**, 667
- Ibata R. A., Malhan K., Martin N. F., 2019b, *ApJ*, **872**, 152
- Jethwa P., et al., 2018, *MNRAS*, **480**, 5342
- Jin S., 2010, *MNRAS*, **408**, L85
- Jones E., Oliphant T., Peterson P., et al., 2001, *SciPy: Open source scientific tools for Python*, <http://www.scipy.org/>
- Kluyver T., et al., 2016, in Loizides F., Schmidt B., eds, *Positioning and Power in Academic Publishing: Players, Agents and Agendas*. pp 87 – 90
- Kroupa P., Theis C., Boily C. M., 2005, *A&A*, **431**, 517
- Kunkel W. E., Demers S., 1976, in *The Galaxy and the Local Group*. p. 241
- Laporte C. F. P., Belokurov V., Koposov S. E., Smith M. C., Hill V., 2019, *MNRAS*, p. L161
- Lauchner A., Powell W. Lee J., Wilhelm R., 2006, *ApJ*, **651**, L33
- Law D. R., Majewski S. R., 2010, *ApJ*, **714**, 229
- Li T. S., et al., 2016, *ApJ*, **817**, 135
- Li T. S., et al., 2019, *MNRAS*, **490**, 3508
- Libeskind N. I., Knebe A., Hoffman Y., Gottlöber S., Yepes G., Steinmetz M., 2011, *MNRAS*, **411**, 1525
- Lovell M. R., Eke V. R., Frenk C. S., Jenkins A., 2011, *MNRAS*, **413**, 3013
- Lynden-Bell D., 1976, *MNRAS*, **174**, 695
- Lynden-Bell D., 1982, *The Observatory*, **102**, 202
- Mackey A. D., van den Bergh S., 2005, *MNRAS*, **360**, 631
- Majewski S. R., Skrutskie M. F., Weinberg M. D., Ostheimer J. C., 2003, *ApJ*, **599**, 1082
- Malhan K., Ibata R. A., Martin N. F., 2018, *MNRAS*, **481**, 3442
- Malhan K., Ibata R. A., Carlberg R. G., Bellazzini M., Famaey B., Martin N. F., 2019, *ApJ*, **886**, L7
- Martin N. F., et al., 2014, *ApJ*, **787**, 19
- Massari D., Koppelman H. H., Helmi A., 2019, *A&A*, **630**, L4
- Mateu C., Read J. I., Kawata D., 2018, *MNRAS*, **474**, 4112
- McKinney W., 2010, in van der Walt S., Millman J., eds, *Proceedings of the 9th Python in Science Conference*. pp 51 – 56
- Metz M., Kroupa P., Jerjen H., 2007, *MNRAS*, **374**, 1125
- Metz M., Kroupa P., Libeskind N. I., 2008, *ApJ*, **680**, 287
- Metz M., Kroupa P., Jerjen H., 2009a, *MNRAS*, **394**, 2223
- Metz M., Kroupa P., Theis C., Hensler G., Jerjen H., 2009b, *ApJ*, **697**, 269
- Müller O., Pawlowski M. S., Jerjen H., Lelli F., 2018, *Science*, **359**, 534
- Myeong G. C., Jerjen H., Mackey D., Da Costa G. S., 2017, *ApJ*, **840**, L25
- Newberg H. J., Yanny B., Willett B. A., 2009, *ApJ*, **700**, L61
- Nidever D. L., Majewski S. R., Butler Burton W., 2008, *ApJ*, **679**, 432
- Nidever D. L., Majewski S. R., Butler Burton W., Nigra L., 2010, *ApJ*, **723**, 1618
- Odenkirchen M., et al., 2001, *ApJ*, **548**, L165
- Odenkirchen M., et al., 2003, *AJ*, **126**, 2385
- Patel E., et al., 2020, arXiv e-prints, p. [arXiv:2001.01746](https://arxiv.org/abs/2001.01746)
- Pawlowski M. S., 2018, *Modern Physics Letters A*, **33**, 1830004
- Pawlowski M. S., Kroupa P., 2013, *MNRAS*, **435**, 2116
- Pawlowski M. S., Kroupa P., 2014, *ApJ*, **790**, 74
- Pawlowski M. S., Kroupa P., 2020, *MNRAS*, **491**, 3042
- Pawlowski M. S., McGaugh S. S., 2014, *ApJ*, **789**, L24
- Pawlowski M. S., Pflamm-Altenburg J., Kroupa P., 2012, *MNRAS*, **423**, 1109
- Pawlowski M. S., et al., 2014, *MNRAS*, **442**, 2362
- Pawlowski M. S., McGaugh S. S., Jerjen H., 2015a, *MNRAS*, **453**, 1047
- Pawlowski M. S., Famaey B., Merritt D., Kroupa P., 2015b, *ApJ*, **815**, 19
- Pawlowski M. S., Bullock J. S., Kelley T., Famaey B., 2019, *ApJ*, **875**, 105
- Peebles P. J. E., 1965, *ApJ*, **142**, 1317
- Perotoni H. D., Martin C., Newberg H. J., Rocha-Pinto H. J., Almeida-Fernandes F. d., Gomes-Júnior A. R., 2019, *MNRAS*, **486**, 843
- Phillips J. I., Cooper M. C., Bullock J. S., Boylan-Kolchin M., 2015, *MNRAS*, **453**, 3839
- Press W. H., Schechter P., 1974, *ApJ*, **187**, 425
- Price-Whelan A. M., 2017, *The Journal of Open Source Software*, **2**, 388
- Price-Whelan A., Sipocz B., Major S., Oh S., 2017, *adrn/gala: v0.2.1*, doi:10.5281/zenodo.833339, <https://doi.org/10.5281/zenodo.833339>
- Reid M. J., Brunthaler A., 2004, *ApJ*, **616**, 872
- Riley A. H., et al., 2019, *MNRAS*, **486**, 2679
- Santos-Santos I. M., Domínguez-Tenreiro R., Pawlowski M. S., 2019, arXiv e-prints, p. [arXiv:1908.02298](https://arxiv.org/abs/1908.02298)
- Shao S., Cautun M., Frenk C. S., Grand R. J. J., Gómez F. A., Marinacci F., Simpson C. M., 2018, *MNRAS*, **476**, 1796
- Shao S., Cautun M., Frenk C. S., 2019, *MNRAS*, **488**, 1166
- Sheffield A. A., Price-Whelan A. M., Tzanidakis A., Johnston K. V., Laporte C. F. P., Sesar B., 2018, *ApJ*, **854**, 47
- Shipp N., et al., 2018, *ApJ*, **862**, 114
- Shipp N., et al., 2019, *ApJ*, **885**, 3
- Simon J. D., 2019, *ARA&A*, **57**, 375

- Sohn S. T., Watkins L. L., Fardal M. A., van der Marel R. P., Deason A. J., Besla G., Bellini A., 2018, *ApJ*, 862, 52
- Starkman N., Bovy J., Webb J., 2019, arXiv e-prints, p. arXiv:1909.03048
- Torrealba G., et al., 2015, *MNRAS*, 446, 2251
- Vasiliev E., 2019, *MNRAS*, 484, 2832
- Villanova S., Monaco L., Moni Bidin C., Assmann P., 2016, *MNRAS*, 460, 2351
- Wang J., Frenk C. S., Cooper A. P., 2013, *MNRAS*, 429, 1502
- Yam W., Carlin J. L., Newberg H. J., Dumas J., O'Malley E., Newby M., Martin C., 2013, *ApJ*, 776, 133
- Yanny B., et al., 2009, *ApJ*, 700, 1282
- Zentner A. R., Kravtsov A. V., Gnedin O. Y., Klypin A. A., 2005, *ApJ*, 629, 219
- van der Walt S., Colbert S. C., Varoquaux G., 2011, *Computing in Science Engineering*, 13, 22

APPENDIX A: SPECIFIC STREAM INFORMATION

Here we describe the choice of anchor points for streams that fall under Class 3 as described in Section 3.2.

20.0-1. This stream was discovered by Mateu et al. (2018) using RR Lyrae found in the Catalina Surveys (Drake et al. 2013a,b; Torrealba et al. 2015). Its member stars nearly span across an entire great circle on the sky in 3 distinct strands. The anchor points are chosen as the closest and furthest RR Lyrae members in heliocentric distance. We take the reported stream width of 1.8 deg for the angular uncertainty and assume a 10% error on the distances.

Cetus. Originally noted by Yanny et al. (2009) and confirmed by Newberg et al. (2009), the Cetus stellar stream was studied in detail by Yam et al. (2013) using blue horizontal branch and red giant stars in SDSS DR8. Its complicated structure is summarized in Table 1 of that paper, which characterizes the spatial and kinematic properties of the stream as a function of binned Galactic latitude; we derive our anchor points from the first and last rows of that table. We use the midpoint of the Galactic latitude bin for the anchor point coordinate, the uncertainty in Galactic longitude for the angular uncertainty of the anchor, and the reported distance d and uncertainty on that distance σ_d for the distance and uncertainty of the anchor.

Corvus. Corvus is the other high-confidence stream candidate discovered by Mateu et al. (2018) using RR Lyrae from the Catalina Surveys. Like the 20.0-1 stream, we use the closest and furthest RR Lyrae members in heliocentric distance for the anchor points. We take the reported stream width of 1.63 deg for the angular uncertainty and assume a 10% error on the distances.

EBS. Originally discovered by Grillmair (2006), the Eastern Banded Structure was re-examined in detail by Grillmair (2011) using the more complete coverage afforded by SDSS DR7. The on-sky positions of the Northern and Southern ends of the stream are not reported explicitly, but can be identified using their Figure 1. We assume an angular uncertainty of 0.5 deg for each endpoint. Distances for each of these endpoints are reported explicitly, as well as the stream width.

Hermus. We base our endpoints for the Hermus stellar stream on the `galstreams` footprint, which is based on the discovery paper (Grillmair 2014). One endpoint is computed using the `galstreams` algorithm, while the other does not match with an end of the stream and is identified separately. Distances for each of these endpoints are reported explicitly in Grillmair (2014), as well as the stream width.

Hyllus. We base our endpoints for the Hyllus stellar stream on the `galstreams` footprint, which is based on the discovery paper (Grillmair 2014). Both endpoints computed using the `galstreams`

algorithm do not match with the ends of the stream footprint and were identified separately. Distances for each of these endpoints are reported explicitly in Grillmair (2014), as well as the stream width.

Kshir. Discovered using *Gaia* DR2 and confirmed spectroscopically by Malhan et al. (2019), the Kshir stream is distinct from but highly correlated in phase space with GD-1. We use two spectroscopic member stars as anchor points, corresponding to the highest ϕ_1 overall and the lowest ϕ_1 star from SDSS. These stars were chosen due to how close they are to the best-fit orbit of Kshir and their high separation from each other. We assume both anchors are at the uncertainty-weighted distance of the stream (10 kpc) with ± 1 kpc uncertainty, while the angular uncertainties are both assumed to be 0.5 degrees.

Kwando. We base our endpoints for the Kwando stellar stream on the `galstreams` footprint, which is based on the discovery paper (Grillmair 2014). Both endpoints computed using the `galstreams` algorithm do not match with the ends of the stream footprint and were identified separately. Grillmair (2017b) reports the FWHM of the stream as 22 arcmin (Gaussian $\sigma = 0.16$ deg) and a physical width of 130 pc, corresponding to a heliocentric distance of 20.3 kpc. We assume both anchor points are at this distance and that the distance uncertainty is 20%.

Magellanic Stream. While the Magellanic Stream has been studied with great detail in recent years (Nidever et al. 2008, 2010), its sheer size and complexity does not easily lend to being described by anchor points. We opt for the anchor points adopted by Pawlowski et al. (2012), which correspond to overdensities identified by Brüns et al. (2005). We adopt the same 55 kpc distance for both anchor points, with a 20% distance uncertainty and an angular uncertainty of 2 degrees.

Murrumbidgee. We base our endpoints for the Murrumbidgee stellar stream on the `galstreams` footprint, which is based on the discovery paper (Grillmair 2014). Both endpoints computed using the `galstreams` algorithm do not match with the ends of the stream footprint and were identified separately. Grillmair (2017b) quotes a heliocentric distance of 20 kpc. We assume both anchor points are at this distance and that the distance uncertainty is 20%.

NGC 5053. Using SDSS data, Lauchner et al. (2006) found a stellar tidal debris stream extending in one direction from globular cluster NGC 5053. We mimic Pawlowski et al. (2012) and use the globular cluster as one anchor point (using spatial data from Harris 1996, 2010 edition) and the quoted end of the stream in Lauchner et al. (2006) as the other. The error in distance to the globular cluster is assumed to be a distance modulus error of 0.1 mag (Vasiliev 2019), while the stream endpoint is assumed to have 20% uncertainty. The angular uncertainty to the cluster is assumed to be zero, while the angular uncertainty to the stream endpoint is assumed to be 1 degree.

NGC 5466. There is a long stellar tidal tail associated with globular cluster NGC 5466 (Grillmair & Johnson 2006). We mimic Pawlowski et al. (2012) and use the globular cluster as one anchor point (using spatial data from Harris 1996, 2010 edition) and the quoted end of the stream in Grillmair & Johnson (2006) as the other. The error in distance to the globular cluster is assumed to be a distance modulus error of 0.1 mag (Vasiliev 2019), while the stream endpoint is assumed to have 20% uncertainty. The angular uncertainty to the cluster is assumed to be zero, while the angular uncertainty to the stream endpoint is assumed to be 2 degrees.

NGC 5904. Using *Gaia* DR2 data, Grillmair (2019) detected a 50° long stream extending westward from NGC 5904 (M5) believed to be the trailing arm. Similar to NGCs 5053 and 5466, we use the globular cluster as one anchor point (using spatial data from Harris

1996, 2010 edition) and the quoted western end of the stream for the other. The error in distance to the globular cluster is assumed to be a distance modulus error of 0.1 mag (Vasiliev 2019), while the stream endpoint is assumed to have 20% uncertainty. The angular uncertainty to the cluster is assumed to be zero, while the angular uncertainty to the stream endpoint is assumed to be 1 degree.

Orinoco. We base our endpoints for the Orinoco stellar stream on the `galstreams` footprint, which refers to Grillmair (2017b). Both endpoints computed using the `galstreams` algorithm do not match with the ends of the stream footprint and were identified separately. Grillmair (2017b) quotes a heliocentric distance of 20 ± 3 kpc. We assume both anchor points are at this distance.

Pal 5. There is a long stellar tidal tail associated with the Pal 5 cluster (Odenkirchen et al. 2001; Grillmair & Dionatos 2006). Recently, Starkman et al. (2019) used Gaia DR2 data to reveal an additional 7 degrees of the leading arm. We use the endpoints quoted in their Figure 4, transformed to (RA, Dec) using the coordinate transformation described in their Appendix B. Both endpoints are assumed to be at the distance to the cluster of 23.2 kpc (Harris 1996, 2010 edition) with distance errors assumed to be 10%.

PAndAS. This stream was discovered as a Milky Way foreground structure in the Pan-Andromeda Archaeological Survey centered on M31 (Martin et al. 2014). We use the overdensity/possible progenitor located at $(l, b) = (117.2, 16.6)$ for one anchor point and the southern end of the stream as the other (Deason et al. 2014). Both anchor points are assumed to be at the average distance to the stream of 17 ± 3 kpc.

Sangarius. We base our endpoints for the Sangarius stellar stream on the `galstreams` footprint, which is based on the discovery paper (Grillmair 2017a). Both endpoints computed using the `galstreams` algorithm do not match with the ends of the stream footprint and were identified separately. We assume both endpoints are at 21 ± 5 kpc (Grillmair 2017b) and that the stream FWHM is 1 deg FWHM (Gaussian $\sigma = 0.422$ deg).

Scamander. We base our endpoints for the Scamander stellar stream on the `galstreams` footprint, which is based on the discovery paper (Grillmair 2017a). Both endpoints computed using the `galstreams` algorithm do not match with the ends of the stream footprint and were identified separately. We assume both endpoints are at 21 ± 5 kpc (Grillmair 2017b) and that the stream FWHM is 1 deg FWHM (Gaussian $\sigma = 0.422$ deg).

APPENDIX B: FULL VERSIONS OF TABLES

This paper has been typeset from a $\text{\TeX}/\text{\LaTeX}$ file prepared by the author.

Name	Type	l_{pole} [deg]	b_{pole} [deg]	Δ_{pole} [deg]	θ_{pred} [deg]	θ_{obs} [deg]	P_{inVPOS}	$P_{>\text{VPOS}}$	$P_{>\text{obs}}$
NGC 104	BD	52.5	-61.7	1.4	51.1	$-80.2^{+0.1}_{-0.1}$	0.000	0.000	0.000
NGC 288	OH	133.2	32.6	8.1	44.7	$49.2^{+4.2}_{-3.0}$	0.000	0.002	0.000
NGC 362	YH	143.7	9.6	15.7	27.0	$29.1^{+2.2}_{-0.9}$	0.946	0.040	0.065
Whiting 1	UN	284.1	-20.8	5.5	43.7	$-67.9^{+3.8}_{-3.4}$	0.000	0.000	0.000
NGC 1261	YH	265.2	39.7	17.2	21.6	$-79.4^{+7.2}_{-14.0}$	0.004	0.038	0.000
Pal 1	BD	183.2	-75.7	1.2	66.9	$73.4^{+0.4}_{-0.5}$	0.000	0.000	0.000
E 1	YH	216.9	36.4	41.0	6.5	$56.9^{+20.7}_{-27.4}$	0.223	0.211	0.086
Eridanus	YH	148.9	27.7	42.6	35.7	$41.5^{+18.2}_{-5.4}$	0.240	0.282	0.288
Pal 2	YH	263.1	-2.9	67.9	84.7	$-86.2^{+2.5}_{-1.4}$	0.000	0.578	0.000
NGC 1851	OH	297.4	18.0	9.3	40.3	$-53.0^{+5.9}_{-3.6}$	0.000	0.003	0.000
NGC 1904	OH	116.0	-4.6	21.2	49.0	$53.2^{+11.9}_{-4.2}$	0.000	0.079	0.021
NGC 2298	OH	134.7	34.2	4.7	41.7	$49.2^{+1.6}_{-1.5}$	0.000	0.000	0.000
NGC 2419	OH	254.4	-32.6	27.6	61.9	$81.3^{+6.2}_{-9.1}$	0.000	0.142	0.003
Pyxis	YH	158.9	9.5	3.7	8.8	$15.9^{+3.2}_{-2.6}$	1.000	0.000	0.000
NGC 2808	OH	90.9	-78.5	6.0	23.1	$85.0^{+3.6}_{-5.9}$	0.000	0.000	0.000
E 3	UN	112.2	-60.2	1.2	25.4	$71.8^{+1.3}_{-1.1}$	0.000	0.000	0.000
Pal 3	YH	164.8	-22.1	28.1	16.6	$26.4^{+16.2}_{-8.8}$	0.753	0.167	0.463
NGC 3201	YH	113.2	62.6	0.5	46.1	$77.7^{+0.5}_{-0.4}$	0.000	0.000	0.000
Pal 4	YH	64.5	15.4	74.8	16.2	$-58.4^{+20.1}_{-29.6}$	0.225	0.362	0.000
Crater	UN	156.3	20.1	75.7	9.4	$49.7^{+26.3}_{-30.4}$	0.347	0.502	0.646
NGC 4147	SG	81.8	16.0	29.5	20.4	$68.9^{+14.9}_{-17.5}$	0.028	0.231	0.000
NGC 4372	OH	119.9	-59.5	1.6	35.9	$68.2^{+1.6}_{-1.4}$	0.000	0.000	0.000
Rup 106	YH	201.5	-44.1	3.0	19.0	$50.2^{+2.7}_{-2.6}$	0.000	0.000	0.000
NGC 4590	YH	207.4	-48.6	1.3	12.8	$56.2^{+0.6}_{-0.6}$	0.000	0.000	0.000
NGC 4833	OH	329.5	-51.1	8.1	29.0	$-56.7^{+5.5}_{-5.8}$	0.000	0.000	0.000
NGC 5024	OH	166.0	-15.0	2.8	12.6	$12.9^{+1.0}_{-0.7}$	1.000	0.000	0.000
NGC 5053	YH	155.9	-13.3	2.2	12.5	$17.1^{+1.1}_{-1.1}$	1.000	0.000	0.000
NGC 5139	UN	323.3	50.4	2.2	39.1	$-52.4^{+2.2}_{-2.1}$	0.000	0.000	0.000
NGC 5272	YH	189.0	-32.3	2.9	31.2	$34.7^{+2.3}_{-2.3}$	0.827	0.000	0.000
NGC 5286	OH	165.4	38.3	5.9	8.0	$41.2^{+5.1}_{-5.9}$	0.227	0.000	0.000
NGC 5466	YH	300.0	18.0	2.3	15.8	$-50.6^{+2.2}_{-1.9}$	0.000	0.000	0.000
NGC 5634	OH	296.6	-22.5	13.8	26.1	$-57.1^{+13.4}_{-9.4}$	0.006	0.014	0.000
NGC 5694	OH	92.6	41.2	18.0	47.3	$79.4^{+7.6}_{-10.0}$	0.000	0.035	0.000
IC 4499	YH	358.3	24.1	2.3	17.7	$-23.0^{+1.8}_{-1.9}$	1.000	0.000	0.000
NGC 5824	OH	33.3	-32.9	3.1	54.7	$-54.9^{+0.5}_{-0.6}$	0.000	0.000	0.000
Pal 5	YH	346.0	-25.1	2.7	28.1	$-28.1^{+1.0}_{-1.0}$	1.000	0.000	0.000
NGC 5897	OH	325.3	-29.9	2.8	24.5	$-40.1^{+2.1}_{-2.4}$	0.101	0.000	0.000
NGC 5904	OH	114.8	-16.0	4.6	25.9	$55.1^{+3.1}_{-2.9}$	0.000	0.000	0.000
NGC 5927	BD	228.4	-81.3	0.7	10.9	$82.8^{+0.5}_{-0.5}$	0.000	0.000	0.000
NGC 5946	OH	190.0	-13.8	6.7	19.0	$23.2^{+5.7}_{-6.4}$	0.993	0.000	0.000
BH 176	BD	298.1	-83.5	1.4	49.5	$-88.7^{+0.8}_{-0.9}$	0.000	0.000	0.000
NGC 5986	OH	0.9	-25.5	9.7	25.2	$-31.1^{+6.3}_{-8.4}$	0.822	0.004	0.000
FSR 1716	UN	6.5	-59.9	2.5	11.5	$-64.2^{+1.4}_{-1.3}$	0.000	0.000	0.000
Pal 14	YH	3.3	-40.1	68.6	32.5	$-48.4^{+24.7}_{-14.1}$	0.252	0.398	0.000
BH 184	BD	349.8	-54.1	3.0	6.8	$-57.1^{+0.9}_{-0.9}$	0.000	0.000	0.000
NGC 6093	OH	26.6	-9.7	6.0	25.3	$-39.4^{+2.2}_{-2.0}$	0.104	0.000	0.000
NGC 6121	OH	275.2	19.4	69.1	73.7	$-77.6^{+8.1}_{-2.5}$	0.000	0.812	0.000
NGC 6101	OH	342.7	53.4	1.4	23.3	$-50.9^{+0.5}_{-0.5}$	0.000	0.000	0.000
NGC 6144	OH	121.3	26.8	3.9	15.0	$54.9^{+2.1}_{-2.0}$	0.000	0.000	0.000
NGC 6139	OH	217.1	-29.4	6.2	34.7	$52.5^{+5.2}_{-6.7}$	0.016	0.000	0.000

Table B1. VPOS membership statistics for all globular clusters analyzed in this work. For column descriptions, see Table 1.

Name	Type	l_{pole} [deg]	b_{pole} [deg]	Δ_{pole} [deg]	θ_{pred} [deg]	θ_{obs} [deg]	P_{inVPOS}	$P_{>\text{VPOS}}$	$P_{>\text{obs}}$
Terzan 3	BD	212.5	-46.3	5.0	3.7	$57.6^{+0.9}_{-0.6}$	0.000	0.000	0.000
NGC 6171	OH	208.7	-35.6	4.7	39.2	$48.9^{+4.0}_{-4.3}$	0.005	0.000	0.000
ESO 452-11	YH	14.7	12.0	20.7	5.9	$-27.2^{+11.5}_{-15.3}$	0.791	0.072	0.000
NGC 6205	OH	243.4	20.3	3.0	44.0	$76.1^{+1.4}_{-1.0}$	0.000	0.000	0.000
NGC 6229	YH	13.9	-11.2	26.6	9.0	$-29.6^{+19.6}_{-16.0}$	0.652	0.104	0.000
NGC 6218	OH	212.9	-51.7	2.5	59.4	$60.8^{+2.2}_{-2.3}$	0.000	0.000	0.000
FSR 1735	UN	207.3	1.9	5.3	37.4	$38.4^{+4.2}_{-5.1}$	0.369	0.000	0.000
NGC 6235	OH	40.6	-39.2	4.6	51.2	$-63.2^{+1.2}_{-1.2}$	0.000	0.000	0.000
NGC 6254	OH	106.7	-52.0	2.5	65.2	$71.3^{+0.2}_{-0.1}$	0.000	0.000	0.000
NGC 6256	BD	223.9	-11.0	6.8	51.6	$54.6^{+4.0}_{-4.2}$	0.000	0.000	0.000
Pal 15	OH	108.5	-8.6	37.9	48.5	$60.0^{+18.5}_{-10.0}$	0.000	0.294	0.087
NGC 6266	OH	169.8	-55.4	7.1	41.4	$52.9^{+4.1}_{-3.9}$	0.000	0.000	0.000
NGC 6273	OH	167.2	24.1	13.2	25.8	$26.7^{+9.3}_{-6.6}$	0.861	0.006	0.038
NGC 6284	OH	268.0	-4.3	7.4	70.9	$-81.6^{+2.5}_{-2.0}$	0.000	0.000	0.000
NGC 6287	OH	262.5	5.3	2.1	33.8	$-86.4^{+2.0}_{-1.9}$	0.000	0.000	0.000
NGC 6293	OH	149.3	45.3	27.3	48.5	$51.7^{+10.6}_{-10.2}$	0.000	0.142	0.070
NGC 6304	BD	139.8	-69.0	2.6	63.1	$69.1^{+2.1}_{-2.5}$	0.000	0.000	0.000
NGC 6316	BD	293.8	-52.6	9.5	68.1	$-72.4^{+1.6}_{-2.6}$	0.000	0.005	0.000
NGC 6341	OH	44.3	-5.1	6.8	41.6	$-55.4^{+5.6}_{-4.6}$	0.000	0.000	0.000
NGC 6325	OH	18.0	17.2	16.0	18.0	$-31.8^{+13.4}_{-9.5}$	0.653	0.019	0.000
NGC 6333	OH	105.2	-29.4	3.0	15.5	$66.2^{+0.5}_{-0.4}$	0.000	0.000	0.000
NGC 6342	BD	79.7	-27.4	3.8	5.7	$87.8^{+1.6}_{-2.7}$	0.000	0.000	0.000
NGC 6356	BD	310.9	-48.8	2.5	59.2	$-61.2^{+1.4}_{-1.7}$	0.000	0.000	0.000
NGC 6355	OH	251.2	17.4	6.7	52.4	$83.1^{+3.4}_{-5.2}$	0.000	0.002	0.000
NGC 6352	BD	51.5	-77.7	1.0	47.0	$-87.1^{+0.5}_{-0.5}$	0.000	0.000	0.000
IC 1257	OH	205.5	68.5	19.1	51.0	$75.0^{+8.5}_{-7.7}$	0.000	0.047	0.003
Terzan 2	BD	31.1	69.3	19.4	37.9	$-71.8^{+2.1}_{-3.8}$	0.000	0.044	0.000
NGC 6366	OH	241.0	-56.2	2.0	76.1	$77.6^{+0.9}_{-0.9}$	0.000	0.000	0.000
Terzan 4	OH	124.1	-34.5	11.9	49.7	$52.5^{+7.5}_{-11.7}$	0.106	0.018	0.003
BH 229	OH	16.4	7.9	37.2	17.8	$-36.8^{+23.0}_{-22.0}$	0.502	0.359	0.000
NGC 6362	OH	124.7	-43.1	3.3	16.5	$56.5^{+3.3}_{-3.1}$	0.000	0.000	0.000
NGC 6380	BD	292.0	76.3	9.9	61.4	$-79.5^{+4.6}_{-4.3}$	0.000	0.003	0.000
Terzan 1	YH	120.8	-76.2	8.8	66.8	$78.3^{+2.3}_{-4.4}$	0.000	0.008	0.001
Ton 2	BD	153.9	-47.6	13.0	7.2	$46.7^{+7.7}_{-6.3}$	0.000	0.013	0.003
NGC 6388	BD	342.9	60.5	4.1	35.4	$-57.9^{+2.9}_{-3.8}$	0.000	0.000	0.000
NGC 6402	OH	36.4	-42.1	4.8	3.3	$-62.1^{+4.5}_{-3.1}$	0.000	0.000	0.000
NGC 6401	OH	262.4	52.6	1.7	61.7	$-86.0^{+1.5}_{-1.2}$	0.000	0.000	0.000
NGC 6397	OH	282.2	-44.7	2.5	71.4	$-76.0^{+1.1}_{-1.0}$	0.000	0.000	0.000
Pal 6	YH	85.1	-3.9	3.5	80.8	$83.9^{+1.3}_{-1.0}$	0.000	0.000	0.000
NGC 6426	YH	14.6	-63.3	3.8	32.5	$-68.7^{+2.9}_{-3.2}$	0.000	0.000	0.000
Djorg 1	UN	125.4	-69.9	5.2	65.1	$72.9^{+1.8}_{-2.0}$	0.000	0.000	0.000
Terzan 5	BD	238.0	-52.3	13.5	74.8	$75.1^{+4.1}_{-6.8}$	0.000	0.025	0.001
NGC 6440	BD	184.5	33.5	16.6	4.2	$39.5^{+7.2}_{-7.6}$	0.377	0.040	0.034
NGC 6441	BD	124.3	-71.0	3.3	68.7	$74.1^{+0.8}_{-1.0}$	0.000	0.000	0.000
Terzan 6	BD	133.4	72.3	11.4	70.5	$78.1^{+1.4}_{-1.8}$	0.000	0.007	0.000
NGC 6453	OH	79.1	-14.5	3.2	74.2	$88.6^{+0.9}_{-1.3}$	0.000	0.000	0.000
NGC 6496	BD	116.1	-59.0	1.7	47.8	$69.6^{+0.5}_{-0.5}$	0.000	0.000	0.000
Terzan 9	YH	249.8	-13.7	10.1	74.5	$79.8^{+6.0}_{-9.2}$	0.000	0.005	0.000
Djorg 2	BD	306.1	-78.5	2.0	84.4	$-84.4^{+1.1}_{-1.7}$	0.000	0.000	0.000
NGC 6517	OH	138.6	-36.7	5.9	17.1	$44.0^{+5.7}_{-5.5}$	0.102	0.000	0.000

Table B2. Continuation of Table B1.

Name	Type	l_{pole} [deg]	b_{pole} [deg]	Δ_{pole} [deg]	θ_{pred} [deg]	θ_{obs} [deg]	P_{inVPOS}	$P_{>\text{VPOS}}$	$P_{>\text{obs}}$
Terzan 10	BD	286.9	-18.6	3.1	57.8	$-65.0^{+1.9}_{-2.7}$	0.000	0.000	0.000
NGC 6522	OH	284.4	-24.8	48.6	43.8	$-70.1^{+4.1}_{-12.5}$	0.061	0.094	0.000
NGC 6535	OH	338.1	68.6	2.6	41.9	$-66.1^{+2.3}_{-2.4}$	0.000	0.000	0.000
NGC 6528	BD	274.2	-16.9	4.2	27.6	$-76.6^{+2.0}_{-1.3}$	0.000	0.000	0.000
NGC 6539	BD	29.9	-33.4	5.8	26.0	$-52.5^{+5.5}_{-4.9}$	0.000	0.000	0.000
NGC 6540	OH	70.1	-66.4	2.0	84.4	$-88.9^{+0.7}_{-1.0}$	0.000	0.000	0.000
NGC 6544	OH	266.5	2.9	7.1	82.5	$-82.7^{+0.2}_{-0.1}$	0.000	0.000	0.000
NGC 6541	OH	53.7	-48.3	5.5	18.6	$-75.7^{+2.6}_{-2.3}$	0.000	0.000	0.000
ESO 280-06	UN	76.2	-19.9	11.3	65.3	$-86.7^{+2.4}_{-4.4}$	0.000	0.004	0.000
NGC 6553	BD	349.9	-82.0	1.5	83.7	$-84.8^{+1.3}_{-1.5}$	0.000	0.000	0.000
NGC 6558	OH	66.2	-20.3	10.1	46.8	$-78.9^{+0.8}_{-0.7}$	0.000	0.000	0.000
Pal 7	BD	102.5	-78.4	0.5	65.6	$82.7^{+0.1}_{-0.2}$	0.000	0.000	0.000
Terzan 12	BD	73.4	-60.3	1.7	89.0	$-89.3^{+0.5}_{-0.8}$	0.000	0.000	0.000
NGC 6569	OH	187.1	-64.6	3.6	59.4	$63.1^{+2.7}_{-3.6}$	0.000	0.000	0.000
BH 261	UN	287.0	-55.0	2.4	73.5	$-77.0^{+1.6}_{-2.2}$	0.000	0.000	0.000
NGC 6584	YH	81.6	-40.9	6.4	42.3	$85.6^{+2.9}_{-2.8}$	0.000	0.004	0.000
NGC 6624	BD	256.4	-15.3	17.2	21.0	$82.9^{+4.9}_{-15.0}$	0.021	0.054	0.000
NGC 6626	OH	259.8	-25.7	5.5	80.9	$88.6^{+1.0}_{-1.8}$	0.000	0.000	0.000
NGC 6638	OH	309.6	-13.3	8.3	22.7	$-42.7^{+7.4}_{-6.0}$	0.169	0.000	0.000
NGC 6637	BD	246.3	-16.0	5.7	13.6	$76.8^{+2.4}_{-1.6}$	0.000	0.000	0.000
NGC 6642	YH	346.3	-29.5	52.0	17.1	$-49.3^{+17.5}_{-26.5}$	0.313	0.351	0.000
NGC 6652	OH	257.0	-17.7	12.8	35.1	$86.6^{+2.0}_{-2.0}$	0.005	0.009	0.001
NGC 6656	OH	270.6	-55.8	1.7	85.2	$-86.0^{+0.1}_{-0.1}$	0.000	0.000	0.000
Pal 8	BD	172.3	-67.9	2.4	39.7	$65.0^{+1.7}_{-1.9}$	0.000	0.000	0.000
NGC 6681	OH	292.4	-4.6	6.3	12.6	$-57.4^{+2.5}_{-3.4}$	0.001	0.001	0.000
NGC 6712	OH	213.9	-6.9	8.7	43.5	$44.4^{+6.7}_{-6.0}$	0.104	0.000	0.000
NGC 6715	SG	274.0	-11.3	2.6	60.4	$-76.2^{+1.2}_{-1.2}$	0.000	0.000	0.000
NGC 6717	OH	324.2	-56.0	4.6	42.7	$-62.4^{+1.8}_{-1.4}$	0.000	0.000	0.000
NGC 6723	OH	31.5	3.5	7.2	1.0	$-42.1^{+2.6}_{-1.4}$	0.000	0.000	0.000
NGC 6749	OH	296.9	-86.5	1.3	31.4	$89.1^{+0.6}_{-0.9}$	0.000	0.000	0.000
NGC 6752	OH	58.7	-65.3	1.3	58.8	$-84.1^{+0.4}_{-0.3}$	0.000	0.000	0.000
NGC 6760	BD	275.8	-83.7	1.1	37.2	$89.0^{+0.7}_{-0.9}$	0.000	0.000	0.000
NGC 6779	OH	22.8	14.3	4.7	34.7	$-35.1^{+1.8}_{-1.3}$	0.845	0.000	0.000
Terzan 7	SG	271.9	-6.0	2.6	53.2	$-77.7^{+1.5}_{-1.5}$	0.000	0.000	0.000
Pal 10	BD	63.1	-82.1	0.6	54.4	$89.4^{+0.4}_{-0.4}$	0.000	0.000	0.000
Arp 2	SG	274.5	-13.8	2.9	51.7	$-75.9^{+1.7}_{-1.8}$	0.000	0.000	0.000
NGC 6809	OH	270.2	-19.9	3.6	60.0	$-80.8^{+1.8}_{-1.5}$	0.000	0.000	0.000
Terzan 8	SG	273.3	-7.8	2.6	48.3	$-76.5^{+1.7}_{-1.8}$	0.000	0.000	0.000
Pal 11	BD	233.5	-63.3	2.4	9.5	$76.1^{+2.2}_{-2.0}$	0.000	0.000	0.000
NGC 6838	BD	48.8	-77.8	0.7	71.4	$-86.6^{+0.5}_{-0.6}$	0.000	0.000	0.000
NGC 6864	OH	159.8	-36.2	18.2	31.5	$35.4^{+6.1}_{-4.0}$	0.593	0.055	0.062
NGC 6934	YH	257.7	-66.4	3.2	6.7	$86.7^{+2.1}_{-2.5}$	0.000	0.000	0.000
NGC 6981	YH	285.2	-37.4	82.9	6.7	$-63.2^{+17.0}_{-31.2}$	0.187	0.569	0.000
NGC 7006	YH	4.9	41.1	23.7	2.6	$-41.5^{+19.5}_{-19.8}$	0.405	0.095	0.000
NGC 7078	YH	272.2	-60.8	3.1	34.4	$-86.1^{+2.4}_{-2.6}$	0.000	0.000	0.000
NGC 7089	OH	170.2	29.5	18.1	24.1	$32.9^{+4.0}_{-4.9}$	0.841	0.054	0.065
NGC 7099	OH	113.0	31.3	11.3	33.0	$63.6^{+9.2}_{-9.9}$	0.005	0.001	0.000
Pal 12	SG	279.3	-22.9	1.9	3.3	$-72.8^{+1.8}_{-2.0}$	0.000	0.000	0.000
Pal 13	YH	46.5	26.8	6.6	25.2	$-59.8^{+5.7}_{-5.6}$	0.000	0.000	0.000
NGC 7492	OH	178.4	3.5	7.9	9.2	$11.8^{+4.4}_{-2.1}$	1.000	0.001	0.141

Table B3. Continuation of Table B1.

Name	Class	RA [deg]	Dec [deg]	Distance [kpc]	$\Delta\theta$ [deg]	Length [deg]	Width [deg]	l_{normal} [deg]	b_{normal} [deg]	θ_{obs} [deg]	P_{inVPOS}	Ref.
20.0-1	3	112.92 273.92	61.56 -43.35	12.6 ± 1.3 28.1 ± 2.8	1.8 1.8	158.6	1.8	270.2	38.0	76.4 ^{+8.3} _{-6.0}	0.000	Mateu et al. (2018)
Acheron	1	230.00 259.00	-2.00 21.00	3.8 ± 0.8 3.5 ± 0.7	0.5 0.5	36.5	0.4	228.2	-53.6	70.4 ^{+6.9} _{-5.1}	0.000	Grillmair (2009)
ACS	1	126.40 133.90	-0.70 64.20	8.9 ± 0.2 8.9 ± 0.2	2.1 2.1	65.1	2.1	143.5	-68.0	67.5 ^{+0.4} _{-0.4}	0.000	Grillmair (2006)
Aliqa Uma	1	31.70 40.60	-31.50 -38.30	28.8 ± 5.8 28.8 ± 5.8	0.3 0.3	10.0	0.3	171.3	23.8	29.9 ^{+13.5} _{-5.3}	0.717	Shipp et al. (2018)
Alpheus	1	27.70 21.58	-45.00 -69.00	2.0 ± 0.7 1.6 ± 0.8	1.4 1.4	24.2	1.4	281.0	-24.1	76.2 ^{+8.7} _{-4.6}	0.000	Grillmair et al. (2013)
ATLAS	1	9.30 30.70	-20.90 -33.20	22.9 ± 4.6 22.9 ± 4.6	0.2 0.2	22.6	0.2	157.4	21.3	28.4 ^{+5.9} _{-3.5}	0.909	Shipp et al. (2018)
Cetus	3	20.01 31.97	-4.12 23.61	32.5 ± 1.3 27.2 ± 1.7	3.5 4.7	30.1	9.4	243.1	1.7	73.9 ^{+4.5} _{-4.5}	0.000	Yam et al. (2013)
Chenab	1	319.30 331.70	-59.90 -43.00	39.8 ± 8.0 39.8 ± 8.0	0.7 0.7	18.5	0.7	208.8	-22.1	43.0 ^{+5.8} _{-6.5}	0.170	Shipp et al. (2018)
Cocytos	1	186.00 259.00	-3.00 20.00	11.0 ± 2.0 11.0 ± 2.0	0.5 0.5	75.1	0.3	164.5	-25.8	25.4 ^{+7.0} _{-6.3}	0.931	Grillmair (2009)
Corvus	3	84.98 266.16	-16.95 -22.06	3.2 ± 0.3 19.4 ± 1.9	1.6 1.6	141.0	1.6	270.2	56.7	77.5 ^{+8.0} _{-7.5}	0.000	Mateu et al. (2018)
EBS	3	132.25 135.40	13.60 0.12	9.4 ± 1.4 9.7 ± 0.9	0.5 0.5	13.8	0.2	181.0	-71.2	68.7 ^{+5.8} _{-6.6}	0.000	Grillmair (2011)
Elqui	1	10.70 20.60	-36.90 -42.40	50.1 ± 10.0 50.1 ± 10.0	0.5 0.5	9.4	0.5	159.6	0.0	14.1 ^{+12.7} _{-7.5}	0.959	Shipp et al. (2018)
Fimbulthul	2	198.74 214.23	-29.56 -22.76	4.2 ± 0.0 4.2 ± 0.0	0.5 0.5	15.5	-	135.5	-44.5	51.2 ^{+0.3} _{-0.3}	0.000	Ibata et al. (2019b)
Fjörm	2	197.37 250.88	5.55 64.20	4.9 ± 0.1 4.9 ± 0.1	0.5 0.5	69.8	-	219.7	-53.1	65.1 ^{+0.3} _{-0.3}	0.000	Ibata et al. (2019b)
Gaia-1	1	184.00 197.00	-18.00 -2.00	6.0 ± 0.6 5.0 ± 0.5	0.5 0.5	20.5	0.5	171.5	-54.6	51.9 ^{+9.3} _{-7.1}	0.001	Malhan et al. (2018)
Gaia-2	1	6.00 15.00	-22.00 -27.00	13.0 ± 1.3 10.0 ± 1.0	0.5 0.5	9.6	-	120.3	22.4	54.0 ^{+6.1} _{-8.6}	0.004	Malhan et al. (2018)
Gaia-3	1	171.00 179.00	-15.00 -32.00	9.0 ± 0.9 14.0 ± 1.4	0.5 0.5	18.5	-	228.2	-58.6	71.7 ^{+3.6} _{-4.4}	0.000	Malhan et al. (2018)
Gaia-4	1	163.00 167.00	-11.00 -3.00	11.5 ± 1.1 10.7 ± 1.1	0.5 0.5	8.9	-	164.4	-41.0	39.7 ^{+14.5} _{-7.6}	0.398	Malhan et al. (2018)
Gaia-5	1	137.00 154.00	23.00 42.00	20.5 ± 2.0 18.5 ± 1.9	0.5 0.5	23.7	-	137.6	-42.8	49.1 ^{+0.9} _{-0.8}	0.000	Malhan et al. (2018)
GD-1	1	135.00 190.00	17.00 58.00	6.5 ± 0.7 10.0 ± 1.0	0.5 0.5	57.4	0.2	120.8	-47.1	61.0 ^{+1.0} _{-1.0}	0.000	Malhan et al. (2018)
Gjöll	2	70.16 90.05	-2.46 -20.15	3.4 ± 0.1 3.4 ± 0.1	0.5 0.5	26.3	-	299.2	-69.6	79.8 ^{+0.7} _{-0.8}	0.000	Ibata et al. (2019b)
Hermus	3	245.40 253.05	5.00 49.90	19.0 ± 3.0 15.0 ± 3.0	0.5 0.5	45.4	0.3	238.0	35.1	74.4 ^{+3.5} _{-4.6}	0.001	Grillmair (2014)
Hyllus	3	249.00 246.90	11.00 34.00	23.0 ± 3.0 18.5 ± 3.0	0.5 0.5	23.1	0.2	253.2	39.3	87.0 ^{+2.0} _{-2.7}	0.000	Grillmair (2014)
Indus	1	323.70 352.00	-50.70 -64.80	16.6 ± 3.3 16.6 ± 3.3	0.8 0.8	20.3	0.8	141.2	-18.5	33.3 ^{+12.1} _{-18.0}	0.598	Shipp et al. (2018)
Jet	1	134.67 142.33	-26.58 -17.53	28.6 ± 0.8 28.6 ± 0.8	0.2 0.2	11.5	0.2	150.6	-14.8	22.0 ^{+0.9} _{-0.6}	1.000	Jethwa et al. (2018)
Jhelum	1	321.20 4.70	-45.10 -51.70	13.2 ± 2.6 13.2 ± 2.6	1.2 1.2	29.2	1.2	298.4	7.4	51.2 ^{+8.5} _{-17.8}	0.186	Shipp et al. (2018)
Kshir	3	230.38 153.05	68.17 25.11	10.0 ± 1.0 10.0 ± 1.0	0.5 0.5	62.1	-	532.3	-57.5	54.9 ^{+1.4} _{-1.2}	0.000	Malhan et al. (2019)
Kwando	3	19.00 31.00	-23.90 -29.33	20.3 ± 4.1 20.3 ± 4.1	0.5 0.5	12.0	0.2	151.6	24.3	36.2 ^{+11.4} _{-5.4}	0.535	Grillmair (2017b)
Leiptr	2	61.03 96.18	0.72 -34.21	7.9 ± 0.4 7.9 ± 0.4	0.5 0.5	48.0	-	151.3	69.2	73.0 ^{+0.9} _{-0.8}	0.000	Ibata et al. (2019b)
Lethe	1	258.00 171.00	20.00 18.00	13.4 ± 2.7 12.2 ± 2.4	0.5 0.5	81.2	0.2	504.1	-30.4	37.1 ^{+4.8} _{-4.0}	0.477	Grillmair (2009)
Magellanic	3	355.93 5.44	-11.91 -27.34	55.0 ± 11.0 55.0 ± 11.0	2.0 2.0	17.8	-	179.3	2.9	12.4 ^{+8.2} _{-4.1}	0.988	Brüns et al. (2005)
Molonglo	1	6.40 13.60	-24.40 -28.10	22.9 ± 4.6 22.9 ± 4.6	0.3 0.3	7.4	0.3	152.3	17.1	35.5 ^{+17.3} _{-12.2}	0.528	Shipp et al. (2018)
Murrumbidgee	3	358.71 13.90	15.97 -25.27	20.0 ± 4.0 20.0 ± 4.0	0.5 0.5	43.8	0.2	201.4	22.0	40.1 ^{+5.2} _{-3.3}	0.162	Grillmair (2017b)
NGC 5053	3	199.11 195.00	17.70 15.00	17.4 ± 0.8 17.4 ± 3.5	0.0 1.0	4.8	-	517.9	-13.7	39.2 ^{+20.2} _{-21.3}	0.467	Lauchner et al. (2006)
NGC 5466	3	211.37 180.00	28.53 42.00	16.0 ± 0.7 16.0 ± 3.2	0.0 2.0	28.7	0.6	276.4	13.0	72.9 ^{+2.8} _{-3.0}	0.000	Grillmair & Johnson (2006)

Table B4. The full list of streams analyzed in this work. For column descriptions, see Table 3.

Name	Class	RA [deg]	Dec [deg]	Distance [kpc]	$\Delta\theta$ [deg]	Length [deg]	Width [deg]	l_{normal} [deg]	b_{normal} [deg]	θ_{obs} [deg]	P_{inVPOS}	Ref.
NGC 5904	3	229.64 190.00	2.08 20.26	7.5 ± 0.3 7.5 ± 1.5	0.0 1.0	42.7	0.7	290.1	13.9	$59.4^{+6.4}_{-9.2}$	0.018	Grillmair (2019)
Orinoco	3	0.00 22.97	-25.51 -28.61	20.0 ± 3.0 20.0 ± 3.0	0.5 0.5	20.7	0.3	131.3	14.8	$41.8^{+6.6}_{-8.4}$	0.267	Grillmair (2017b)
Orphan	1	145.00 153.00	40.00 20.00	38.0 ± 3.8 33.0 ± 3.3	0.5 0.5	21.1	2.0	210.7	-45.4	$55.9^{+2.2}_{-2.3}$	0.000	Malhan et al. (2018)
Pal 5	3	219.36 239.69	-12.02 5.84	23.2 ± 2.3 23.2 ± 2.3	0.5 0.5	27.0	0.3	172.4	28.2	$31.4^{+1.7}_{-1.8}$	1.000	Starkman et al. (2019)
Palca	1	30.30 16.20	-53.70 2.40	36.3 ± 7.3 36.3 ± 7.3	0.8 0.8	57.3	0.8	205.9	20.4	$42.7^{+3.0}_{-2.7}$	0.015	Shipp et al. (2018)
PAndAS	3	4.95 20.47	45.92 40.97	17.0 ± 3.0 17.0 ± 3.0	0.5 0.5	12.3	1.0	196.8	65.8	$71.5^{+4.7}_{-6.0}$	0.000	Martin et al. (2014)
Pegasus	1	328.30 333.40	20.80 28.10	18.0 ± 2.0 18.0 ± 2.0	0.2 0.2	8.6	0.2	233.0	-52.3	$72.4^{+6.4}_{-15.3}$	0.041	Perotoni et al. (2019)
Phlegethon	2	284.75 324.50	-59.20 -0.26	3.6 ± 0.3 3.6 ± 0.3	1.4 1.4	66.6	1.4	526.4	72.9	$75.8^{+1.2}_{-1.3}$	0.000	Ibata et al. (2018)
Phoenix	1	20.10 27.90	-55.30 -42.70	19.1 ± 3.8 19.1 ± 3.8	0.2 0.2	13.6	0.2	235.6	29.2	$71.4^{+9.9}_{-23.3}$	0.098	Shipp et al. (2018)
PS1-A	2	28.39 30.14	-6.55 -1.97	7.9 ± 1.9 7.9 ± 1.9	0.5 0.5	4.9	0.2	249.3	22.9	$81.4^{+5.8}_{-14.7}$	0.000	Bernard et al. (2016)
PS1-B	2	145.59 151.13	-15.28 -7.00	14.5 ± 3.4 14.5 ± 3.4	0.5 0.5	9.9	0.2	144.0	-24.2	$42.1^{+16.9}_{-9.6}$	0.348	Bernard et al. (2016)
PS1-C	2	330.26 334.98	11.75 18.20	17.4 ± 4.0 17.4 ± 4.0	0.5 0.5	7.9	0.1	238.2	-46.1	$75.6^{+9.3}_{-24.8}$	0.072	Bernard et al. (2016)
PS1-D	2	138.70 140.74	-21.58 23.28	22.9 ± 5.3 22.9 ± 5.3	0.5 0.5	44.9	0.4	164.8	-52.6	$49.9^{+3.8}_{-3.1}$	0.000	Bernard et al. (2016)
PS1-E	2	160.11 192.94	46.13 62.89	12.6 ± 3.0 12.6 ± 3.0	0.5 0.5	24.9	0.3	158.4	-52.8	$52.5^{+5.1}_{-3.4}$	0.000	Bernard et al. (2016)
Ravi	1	334.80 344.00	-44.10 -59.70	22.9 ± 4.6 22.9 ± 4.6	0.7 0.7	16.6	0.7	170.6	-14.9	$18.1^{+11.3}_{-5.1}$	0.930	Shipp et al. (2018)
Sangarius	3	134.06 131.57	-17.79 32.65	21.0 ± 5.0 21.0 ± 5.0	0.5 0.5	50.5	0.4	164.2	-60.6	$57.8^{+3.0}_{-2.1}$	0.000	Grillmair (2017a)
Scamander	3	151.64 143.61	-20.47 44.34	21.0 ± 5.0 21.0 ± 5.0	0.5 0.5	65.2	0.4	187.4	-54.9	$54.1^{+3.4}_{-2.5}$	0.000	Grillmair (2017a)
Slidr	2	148.38 178.01	14.99 2.98	3.6 ± 0.1 3.6 ± 0.1	0.5 0.5	31.6	-	273.1	-21.5	$78.3^{+0.7}_{-0.8}$	0.000	Ibata et al. (2019b)
Styx	1	259.00 194.00	21.00 20.00	50.0 ± 10.0 38.0 ± 7.6	1.4 1.4	60.4	1.4	499.6	-2.1	$29.7^{+2.3}_{-2.7}$	0.996	Grillmair (2009)
Svöl	2	244.44 248.73	23.37 40.94	7.8 ± 0.2 7.8 ± 0.2	0.5 0.5	17.9	-	230.3	3.9	$61.2^{+4.7}_{-5.5}$	0.000	Ibata et al. (2019b)
Sylgr	2	167.79 186.58	-8.35 -1.26	4.1 ± 0.0 4.1 ± 0.0	0.5 0.5	20.0	-	299.8	29.9	$54.1^{+0.2}_{-0.2}$	0.000	Ibata et al. (2019b)
Triangulum/Pisces	1	21.35 23.98	34.98 23.20	26.0 ± 4.0 26.0 ± 4.0	0.5 0.5	12.0	0.2	222.2	24.6	$58.5^{+2.8}_{-1.6}$	0.000	Bonaca et al. (2012)
Tucana III	1	353.70 3.20	-59.70 -59.40	25.1 ± 5.0 25.1 ± 5.0	0.2 0.2	4.8	0.2	286.0	25.4	$69.0^{+5.9}_{-18.4}$	0.095	Shipp et al. (2018)
Turbio	1	28.00 27.90	-61.00 -46.00	16.6 ± 3.3 16.6 ± 3.3	0.2 0.2	15.0	0.2	209.0	32.4	$52.5^{+16.2}_{-22.7}$	0.248	Shipp et al. (2018)
Turranburra	1	59.30 75.20	-18.00 -26.40	27.5 ± 5.5 27.5 ± 5.5	0.6 0.6	16.9	0.6	155.4	42.5	$47.0^{+5.7}_{-3.3}$	0.000	Shipp et al. (2018)
Wambelong	1	90.50 79.30	-45.60 -34.30	15.1 ± 3.0 15.1 ± 3.0	0.4 0.4	14.2	0.4	183.5	61.9	$65.1^{+10.3}_{-17.3}$	0.007	Shipp et al. (2018)
Willka Yaku	1	36.10 38.40	-64.60 -58.30	34.7 ± 6.9 34.7 ± 6.9	0.2 0.2	6.4	0.2	229.9	33.0	$67.8^{+12.1}_{-29.9}$	0.152	Shipp et al. (2018)
Ylgr	2	169.05 182.65	-10.36 -37.12	9.5 ± 0.3 9.5 ± 0.3	0.5 0.5	29.4	-	184.2	-52.0	$50.8^{+2.3}_{-2.5}$	0.000	Ibata et al. (2019b)

Table B5. Continuation of Table B4.